






Article

An Analysis on the VSC-HVDC Contribution for the Static Voltage Stability Margin and Effective Short Circuit Ratio Enhancement in Hybrid Multi-Infeed HVDC Systems

Diego Oliveira ¹, Gustavo C. Borges Leal ¹, Danilo Herrera ², Eduardo Galván-Díez ², Juan M. Carrasco ^{2,*}
and Mauricio Aredes ¹

¹ Electrical Engineering Department, Federal University of Rio de Janeiro, Rio de Janeiro 21941-598, Brazil

² Departamento de Tecnología Electrónica, Universidad de Sevilla, 41092 Sevilla, Spain

* Correspondence: jmcarrasco@us.es

Abstract: Over the years, high voltage transmission of large energy blocks over long distances has widely developed from the Line Commutated Converter (LCC) technology. However, the continuous expansion of the AC network and the increase in renewable energy penetration leads to the weakening of Electric Power Systems (EPS), causing operational problems for the LCC-HVDC. This paper evaluates the degree of contribution of the VSC-HVDC on the LCC-HVDC dynamic performance when the infeed is in a hybrid multi-infeed HVDC system. Through a steady-state mathematical framework, the new concept of Hybrid Power Voltage Interaction Factor (*h*PVIF) is proposed to assess the transient stability improvement of LCC. Additionally, this article introduces two key contributions from *h*PVIF: the complementary Improved Commutation Failure Immunity Index (*i*CFII), as a measure of the effective short circuit enhancement, as well as the apparent line length, which emulates the line lengths adjusting the power dispatch in the VSC-HVDC. PSCAD/EMTDCTM time-domain dynamic simulations are performed to assess the indexes, and the Matlab[®] software will be used to assist in mathematical operations.



Citation: Oliveira, D.; Leal, G.C.B.; Herrera, D.; Galván-Díez, E.; Carrasco, J.M.; Aredes, M. An Analysis on the VSC-HVDC Contribution for the Static Voltage Stability Margin and Effective Short Circuit Ratio Enhancement in Hybrid Multi-Infeed HVDC Systems. *Energies* **2023**, *16*, 532. <https://doi.org/10.3390/en16010532>

Academic Editor: Abdelali El Aroudi

Received: 26 November 2022

Revised: 24 December 2022

Accepted: 28 December 2022

Published: 3 January 2023



Copyright: © 2023 by the authors. Licensee MDPI, Basel, Switzerland. This article is an open access article distributed under the terms and conditions of the Creative Commons Attribution (CC BY) license (<https://creativecommons.org/licenses/by/4.0/>).

Keywords: hybrid multi-infeed system (HMIF); improved commutation failure immunity index (*i*CFII); hybrid power voltage interaction factor (*h*PVIF)

1. Introduction

The LCC-HVDC technology has played a crucial role in Brazilian's National Inter-connected System (SIN) in the exchange of large blocks of energy over long distances. The Brazilian scenario in 2022 contains four HVDC links feeding 20 GW in the Southeast area, two 600 kV bipoles of Itaipu, two 600 kV bipoles of Madeira, and two UHVDC 800 kV bipoles of Belo Monte. In the so-called decennial publication SIN Expansion Plan, the government agency responsible for Brazilian energy planning indicates three more ± 800 kV UHVDC links for subsequent years. They are: the bipoles of Graça Aranha–Silvânia link (1460 km, 4000 MW), the Parauapebas–Assis link (1940 km, 4000 MW) to be in operation until 2023, and a third UHVDC link is under study to transport energy from the Tapajós power plant to the Southeast, with 8000 MW for two bipoles (1500 and 2500 km) in the entire operation from 2027 [1].

In the medium-term perspective, systemic insertion of renewable energy sources added to an increase in the AC transmission lines integrating the primary grid [2], pointing out the consequent weakening of the EPS, thus aggravating issues when LCC-HVDC are connected. Brazil has a large territorial dimension and an energy matrix in which the main generation plants are located far from load centers. Additionally, environmental constraints are reducing the Right of Way (RoW) permission for overhead lines, therefore collaborating to change power systems' characteristics, becoming more interconnected and reliable, but with new, complex paradigms. This highlights the emergence of some notable

technical challenges in LCC-HVDC systems, leading to increased Commutation Failures (CF) susceptibility, for instance. Thus, new actions to meet power requirements, such as higher reactive support, became necessary to overcome problems caused by AC voltage reduction at the inverter side bus.

In this context, the literature contains published works analyzing these challenges of LCC-HVDC operation and proposing solutions for enhancing commutation failure immunity and improving the overall reliability of the interaction between AC and DC systems, with special attention given to weak networks. According to the nature of CF, there are three technical routes for CF prevention and mitigation CF. They are improvements to primary equipment, new control strategies for LCC-HVDC and reactive support in the AC side of the inverter. Throughout the literature review, some of the main references in each of these methods will be cited and briefly commented.

In [3,4], the authors considered the insertion of voltage control equipment in the vicinity of the LCC-HVDC. The AC system strength and control models assessment was considered in reference [5,6], and employing thyristor-based controllable capacitors to eliminate CF was considered in [7–9].

Advanced control methods for preventing and mitigating the consequences of commutation failure have developed in the second decade of the 21st century, such as those with real-time measurement and calculation of inverter quantities, such as extinction angle, AC commutation voltage, DC current, and overlap area of the thyristor voltage waveforms, in order to anticipate control actions and inhibit CF [10–14].

Modern electrical power systems worldwide have expanded using Voltage-Sourced Converter-based High-Voltage Direct Current (VSC-HVDC) transmission links, which recently was just an emerging technology in the HVDC area. However, its application in transmitting large energy blocks over long distances has increased due to the development of self-commutated devices operating at higher voltage rates and economic competitiveness compared to LCC technology. More recently, the authors of [15] introduced a control strategy to overcome the disadvantages inherent to conventional LCC systems, combining the VSC and LCC converters. The author detailed the VSC-HVDC link contribution to voltage stability, proposing a flexible power control strategy for transitory reactive power under grid faults. The studies combining VSC and LCC operating in the same AC system and the analysis of the interactions that arise from it contributed to doctoral theses, such as [16–19].

A few recent works are devoted to discussing the VSC-HVDC in its principal function, which is point-to-point power blocks transmission in a controlled way [20,21]. Other publications bring positive results in the performance improvement of the LCC-HVDC when a VSC-HVDC operates in their geographic proximity. Some papers discussed the VSC-HVDC control modes at length, mainly when operating within a multi-infeed system [22–25], in both transient and steady-state performance.

To partially finish the literature review, an influential group of articles forms one of the bases of this work, and the beginning of developing methods for the analysis and simulation of Electric Power Systems (EPS) in the vicinity of the voltage stability limit [26] will be presented. The study of AC/DC interactions phenomena in low short-circuit capacities systems began with [27], where methods based on the eigenvalue decomposition technique for analyzing the voltage stability of multi-infeed systems were presented. Similar techniques for power and voltage stability in MIF systems have been established since then and developments continue to this day [28,29].

An exhaustive framework on two essential nodal AC voltage indices applied to the voltage interaction studies in multi-infeed systems was presented in [30]. The author has compared the respective indices obtained empirically on related literature. It investigated the *NVSF* and the *NVIF* and compared them with their counterparts obtained through simulations in electromagnetic transient programs *VSF* and *MIIF*, respectively. However, this study is restricted to those MIF scenarios composed purely of LCC-HVDC links.

A more innovative approach focuses on examining the relationship between DC power stability and voltage sensitivity of the inverter [31], calculating the Effective Short Circuit Ratio (ESCR) to predict the maximum power transfer limit in hybrid MIF systems [32]. Analytical formulation of voltage interactions between inverters in hybrid MIF systems is further explored in [33].

Thus far, journal articles and doctoral theses have been listed, forming this bibliographic review's basis. However, a valuable group of conference papers is dedicated to dealing with multi-infeed systems, including hybrids and their main issues involving their operation in low ESCR systems and mitigation of CF. Some of them deserve mention here. A large amount of computational electromagnetic simulations is performed in [34,35] to analyze the coupling effect between VSC and LCC, and the commutation failure mechanism of the LCC-HVDC system. The mathematical approach for CF immunity level assessment is also presented in [36–40].

Some primary bibliographic references have been placed from a historical perspective. The other references will be listed and commented on within their respective sections throughout the article.

These works address different solutions for quantifying commutation failure immunity levels and enhancements in CF immunity. These publications provided valuable contributions to the field and advanced the state-of-the-art of LCC-HVDC performance improvement. However, such advances were restricted to scenarios of single-infeed HVDC systems or multi-infeed HVDC systems composed purely by LCC links. In addition, some of them use simulation tools as a fundamental basis to reach results, which inevitably take a long time and result in computational burden. Until today, no other work considers hybrid MIF with LCC and VSC links exploring the cross effects resulting from the power–voltage relation between them, especially provided when a tie line transmission line connects these links, thus resembling real scenarios.

This work aims to provide a systematic and generally applicable method for stability analysis of hybrid multi-infeed HVDC systems from which the sensitivity of the system parameters on the ESCR in the inverter side can be precisely and effectively determined. By including LCC-HVDC equations into power flow with power injection formulation and based on the eigenvalue decomposition technique, analytical expressions are derived from giving an insight into how inter-inverter interactions influence the transient performance of LCC-HVDC systems.

The investigations performed in this manuscript show that strengthening the AC system is highly influenced by VSC operation and location. Geometrically, it is observed that such influence assumes the form of a surface, where the voltage in the LCC and, therefore, its ESCR behave in different ways for the variations of active and reactive VSC powers. The variation of active VSC power produces a parabola with a well-defined global maximum point and an approximately linear characteristic in the direction of the variation of VSC reactive power. Here arises the main motivation for this work. The gradient of a two-dimensional function is applied to map how the VSC impacts the LCC-HVDC voltage stability. The contributions of the work are summarized below:

- Hybrid Power Voltage Interaction Factor ($hPVIF$): As the primary contribution, the factor $hPVIF$ is proposed. From the power–voltage relationship between the LCC and VSC links, and given the length of the transmission line that connects the inverter buses, $hPVIF^p$ allows extracting the system operation set point necessary to achieve the maximum ESCR in the LCC link. Knowledge of this point, therefore, includes knowing how far the VSC must be connected from the LCC and setting the values of the active and reactive power coordinates in the VSC for the upper limit for the voltage stability margin in the LCC inverter station. Factor $hPVIF^q$ is helpful for the further contribution of the manuscript, i.e., apparent line length; therefore, $hPVIF^p$ and $hPVIF^q$ complement each other to achieve the objectives of this work.
- Among the stability problems in LCC systems, commutation failure is the most common and undesirable problem and will be adopted as a predictor instrument of

the ESCR gain assessment. Based on CFII, which will be discussed in detail from Section 2 onwards, the new metric Improved Commutation Failure Immunity Index (*i*CFII) is specifically designed to evaluate the ESCR enhancement compared to the situation without the presence of the VSC.

- A method for incorporating the equations representing the steady-state response of the LCC-HVDC inverter into the power flow problem formulation is described (Section 3.3). The control mode and its impact on the power system operating conditions are addressed so that it results in an extended Jacobian for hybrid multi-feed systems.
- The electrical system operators' decisions in the operation programming process are carried out daily, monthly, and annually. In all cases, the programming considers systemic aspects, such as the generation and transmission expansion schedule, the level of the reservoirs, load forecasts, analysis of meteorological conditions in the main river basins of the EPS, and forecasts of inflows to the hydroelectric uses. In this context, as these are aspects closely related to medium and long-term horizons and, therefore, with little or no flexibility for short-term changes, the operation agents need to have a reliable instrument that allows emulating a more advantageous value for the ESCR seen by a given LCC-HVDC. From the proper choice of VSC-HVDC set points, the apparent line length concept presented in Section 5.1.2 allows for the emulation of a shorter line length than the actual length, resulting in a higher value of ESCR.

The outline of the paper is as follows. After the Introduction, Section 2 reviews aspects of the LCC-HVDC operation that influences the CF, in addition to contextualizing the object of study of this article. In the Section 3, a quasi-steady-state mathematical analysis is used to present the main idea with references in the appendix, resulting in the definition of the Hybrid Multi-Infeed Interaction Factor, which is the work's fundamental contribution. In support of the following steps, the Section 4 contains the case study implemented in PSCAD detailing system components and the VSC-HVDC control scheme. The Section 5 shows the simulation outcomes and analysis. Section 6 summarizes the research and concludes the paper based on the previous results.

2. Commutation Failure Analysis

2.1. Commutation Failure: Definition and Past Approaches

Commutation Failure (CF) is an adverse condition of vulnerability, especially due to weak systems, which can cause sustained overcurrents, damaging equipment. The emergence of the commutation failure theory dates back to the early nineties with a formulation proposed for a CF induction mechanism [41,42]. The CF investigations intensified over the next few years, passing through [43,44], which reveals through simulations that the results from such a previous formulation only match those obtained for a set of specific scenarios.

Since fast transient events and unbalances have to be considered in CF studies, the more appropriate way to analyze it is through detailed EMT simulation of the systems [45], and in this way, advances with the most recent works [46,47] were achieved.

The CF consists of an adverse event inherent to thyristor-controlled converters. It is a critical operational fault that severely compromises the system performance as it causes temporary interruption of the power transmitted by the converter, current surges in the key thyristors, and can cause significant disturbances in the operation of the AC network and other converters. For these reasons, it requires adequate protective measures to prevent the system collapse.

After the end of the commutation process between two thyristors, the off-thyristor must remain with a reverse voltage at its terminals for a longer time than the minimum required to complete the deionization of the semiconductor. Due to operational characteristics, commutation failure is more likely to occur in the inverter station. The dominant causes are large fluctuations in DC current (I_d), control failures in the thyristors triggering an instant, transient harmonic distortions, and, especially, voltage disturbances in the AC network.

Although a commutation failure can be due to many causes, the most common is the voltage drop at the inverter station after an AC fault. In the past, some studies have been conducted to quantify the level of voltage drop that could occur on the inverter AC terminal without causing a commutation failure. They have been used to assess an HVDC system's immunity to commutation failure [48]. However, by purely considering voltage magnitude and ignoring phase shifting and wave distortion, it is not enough to accurately determine the critical voltage drop at the inverter AC busbar.

2.2. Minimum Extinction Angle Criteria

In this way, it is appropriate to analyze the valve commutation phenomena from the perspective of the extinction angle, described by the extinction angle equation in (1), which comprises all the process variables. The extinction angle (γ_n) should be greater than ωt_q (usually 7°) for the thyristor that is not conducting to restore its blocking capacity fully. The time t_q corresponds to the safe extinction interval after complete switching of the current I_{dn} under the penalty of commutation failure [49].

$$\gamma_n = \cos^{-1} \left(\frac{\sqrt{2} X_{cn} I_{dn}}{V_n} + \cos \alpha_n \right) \quad (1)$$

Considering commutation voltage at bus n (V_n) as sinusoidal under normal operating conditions and a ripple-free DC current, the commutating reactance is mainly composed of the short-circuit reactance of the converter transformer given by (2), in which V_{nN} represents phase-to-ground three-phase AC bus voltage.

$$X_{cn} = x_{T(pu)} \frac{V_{nN} / (\sqrt{3} n_n)}{\sqrt{2} I_{dnN} / \sqrt{3}} = \frac{x_{t(pu)} V_{nN}}{\sqrt{2} n_n I_{dnN}} \quad (2)$$

Based on the denominator of (1), it can be noted that the susceptibility of CF occurrence is directly related to the AC network and VSC-HVDC parameters. In ideal circumstances, it would be convenient to choose the VSC's powers and the transmission line length so that, under a sudden AC voltage sag, γ_n was not less than a minimum limit, γ_{min} . In other words, for such a line length, if P_k and Q_k could be transiently changed during a contingency, and the corresponding critical parameters of (1) could also be determined so that $\gamma > \gamma_{min}$ is always possible. The fundamental condition concerns the threshold values to ensure $\gamma > \gamma_{min}$ should be reached immediately after a disturbance. However, as will be addressed in Section 2.5, the CF time interval is in the order of μs , and therefore, there is no reason to attempt control over V_k in the first post-fault instants since the controllers and the Phase Locked Loop (PLL) time constants are relatively more extended than the required time intervals for the first fault to occur.

2.3. AC Voltage Interactions: The Critical Indexes

The first systematic studies were conducted in the early nineties [50] and advanced to MIF systems analysis only involving VSC [51].

Among the stability problems in LCC systems, CF is the most common and undesirable adversity in LCC-HVDC systems. It is an operational condition that must be strongly avoided because it leads to a DC voltage short-circuit resulting from the thyristor's pulse sequence of the same leg (opposite pole), with the consequent interruption in power transmission, in addition to causing harmful overcurrents in the thyristor that has restored conduction. Equation (1) indicates that several events motivate CF, such as sharp commutation voltage sags in V_n , an increase in I_d , decreases in β , or even control and triggering failures in the inverter station. However, CF mostly occurs due to the V_n deterioration, which usually justifies the focus on this quantity in this work and other related works.

A particular concern in LCC-HVDC in the MIF configuration is the existing electrical interactions between AC and DC systems. The AC faults in the inverter busbar are critical,

as well as those in electrically close LCC-HVDC inverters, which will cause the so-called concurrent or remote CF.

In this context, the Multi-Infeed Interaction Factor (MIIF) is proposed in [52] as a metric for estimating the level of voltage interaction between two inverter's infeed in the same electrical region. The smaller the distance between them, the higher degree of interaction, and the MIIF is used to reflect the effective interactions among any buses of the MIF system. By definition, the index represents the voltage reduction in the busbar n (V_n) followed by a 1% sudden drop in voltage of the busbar k (V_k), as described in (3).

$$MIIF_{nk} = \frac{\Delta V_n}{\Delta V_k} \quad (3)$$

Essentially, the index denotes how an HVDC link is influenced by another, playing a key role in studying the safe and stable operation of the whole EPS. Generally, for two buses infinitely far apart, $MIIF = 0$ and $MIIF = 1$ if two buses are connected to the same AC bus. If two LCC-HVDC have the same ratings, the interactions for $MIIF \leq 0.15$ could be ignored, and each link behavior as a single-infeed system.

There are some ways of equating the MIIF [53] considering grid parameters, for which knowledge of the admittance matrix is required. Equation (4) shows the analytical result. The impedance Z_{nk} is the interconnection impedance between the buses n and k , and Z_{kk} is the sum of the impedance connected to the bus k .

$$MIIF_{nk} = \left| \frac{Z_{nk}}{Z_{kk}} \right| \quad (4)$$

Dynamics simulations could be applied to reach a more precise measure of MIIF [54], in which the admittance matrix is not required. In practice, a variation of 1% at bus k is performed by switching a shunt inductance, and the resulting voltage V_n is observed.

2.4. The AC System Strength: Short Circuit Ratio Index

This section discusses the main index regarding schemes with multiple LCC-HVDC links in the same AC network area. The Short-Circuit Ratio (SCR) is defined in (5) in which S_{sc_n} is the short circuit capacity of the AC network at the AC busbar with all remaining converters blocked divided by the MW rating of the n th HVDC scheme (P_{dn}). Once the Thévenin equivalent impedance (Z_{nn}) is known, the SCR_n can still be written in terms of this normalized impedance expressed per unit.

$$SCR_n = \frac{S_{sc_n}}{P_{dn}} = \frac{\sqrt{3}V_n I_{sc}}{P_{dn}} = \frac{V_n^2 / Z_{nn}}{P_{dn}} = \frac{1}{Z_{nn}(pu)} \quad (5)$$

In practice, S_{sc_n} is the short-circuit power of a symmetrical three-phase metallic fault at converter bus n , and Z_{nn} is measured by looking into the AC grid from the commutation AC bus at the fundamental frequency. Another meaningful and widely used indicator of the AC system strength is the Effective Short-Circuit Ratio (ESCR), calculated taking into account the reactive support at the n AC busbar (Q_{C_n}). The $ESCR_n$ definition is given in (6). In this case, the capacity of VSC-HVDC (S_{VSC}) can also be considered.

$$ESCR_n = \frac{S_{sc_n} + S_{VSC} - \sum Q_{C_n}}{P_{DC_n}} \quad (6)$$

In an MIF scenario where two or more LCC-HVDC inverters are connected in different but electrically close points in a restricted location, planning agencies must pay special attention mainly in low SCR conditions, when interaction amongst the links is likely to occur. In this context, the ESCR acts as a valuable predictor of the degree of the following interactions of concern [55]:

- Commutation failure including the effects of its propagation,

- Power and voltage instability,
- Requirements on recovery control coordination during AC and DC faults,
- Transitory overvoltage (TOV),
- Resonances and harmonic interaction,
- Requirements on coordination between HVDC controls.

It is important to emphasize that although this article has adopted the CFII as an instrument for the ESCR gain assessment, other parameters related to the weakness of the EPS are also relevant, such as difficulties in the black start, Maximum Available Power (MAP), recovery times in voltage sags, and TOV in load rejection.

2.5. Contextualization: Background and Motivation

Some works have studied the influence of VSC presence on the dynamic support of reactive power when an adverse transient disturbance occurs. In this context, the *i*CFII and its dependence on the VSC-HVDC operation point will be presented. It shows two parameters' effects on CF susceptibility for two scenarios. Firstly, Figure 1a illustrates the LCC response to the CF for two P_k values for the same tie line length. When P_k goes from 0.9 to 0.75 pu, the successive CF evolves to a single fault, which denotes a direct improvement in the ESCR. The CF is extinguished by keeping 0.75 pu and increasing the tie line length to 180 km. Figure 1b shows the improvement in CFII when the line length is increased from 70 to 80 km with a fixed power dispatch. Similar behavior can be noted, and the CF is completely extinguished when the line length reaches 100 km. What can be seen is that an immediate improvement in transient state performances is soon observed connecting the VSC at a given operating point *M*, without any changes to the AC network equivalents in order to maintain the original ESCR.

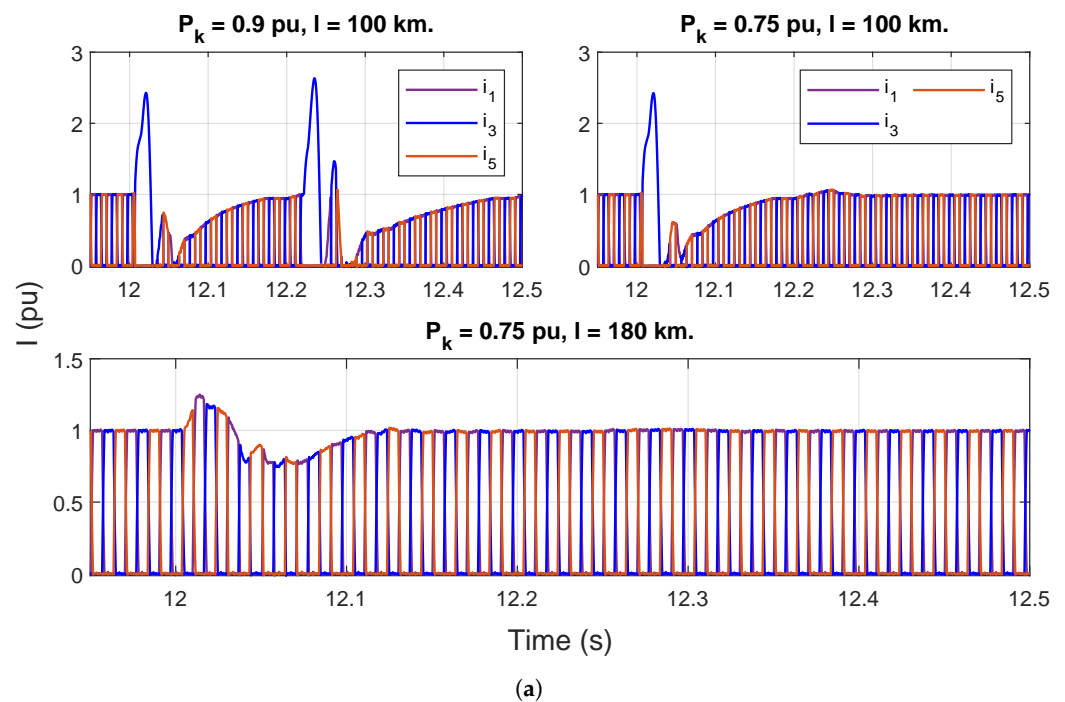


Figure 1. Cont.

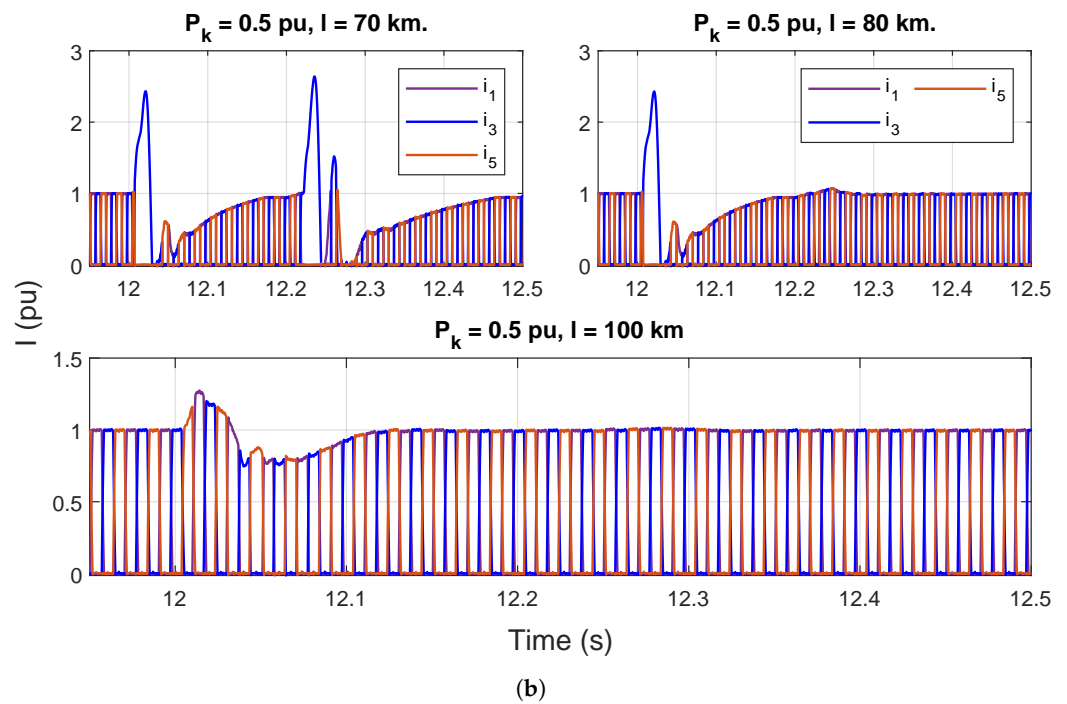


Figure 1. Thyristors currents i_1 , i_3 and i_5 as a function of VSC power dispatch and tie line length: (a) Thyristors currents as function of VSC power dispatch. (b) Thyristors currents as function of VSC-LCC tie line length.

Figure 2 illustrates the characteristic of the probability of CF. It could intuitively suggest that the faster the vector \vec{S} excursion towards maximizing Q_k , the better the voltage support of the VSC in the AC network, $iCFII_3 > iCFII_2 > iCFII_1$. However, the improvement in control performance is observed only for voltage recovery a few seconds after the event. As will be seen in the discussion based on Figure 3, this fact does not affect the performance of the VSC in terms of contributing to avoiding CF.

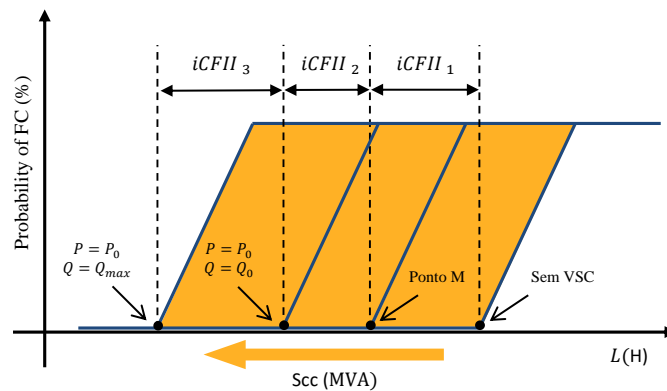


Figure 2. Graphic representation of $iCFII$ gain.

Figure 3a shows a window with detail of Figure 1a, containing all the thyristor currents in the transient time interval of the CF when $P_k = 0.75$ pu for 100 km. It can be seen that commutation failure shows a very short transient. Compared to Figure 3b, which is a one-step in P_k order, it is concluded that no matter how well designed, a power regulator would not be able to prevent the first CF, and it can contribute little or nothing since the resulting closed-loop time constant is 420 ms, that is, more than 70 times greater than the short period of occurrence of the phenomenon.

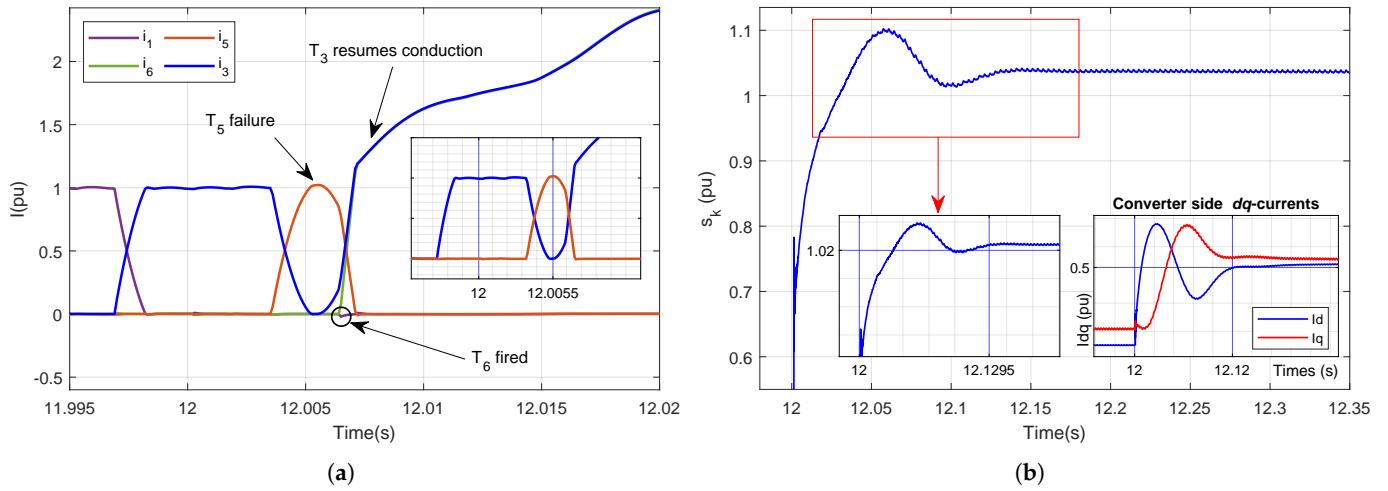


Figure 3. Inverter commutation failure simulation. Dynamic detail: (a) valve currents under commutation failure. (b) VSC Complex power— \vec{S}_k .

These findings indicate that VSC operation and location contribute to strengthening the AC system, which is observed by reducing the probability of CF. In addition, it is more probable that the dynamic contribution of \vec{S} for voltage support is in the coming stages of the CF, i.e., avoiding successive and remote (or concurrent) CF. In other words, VSC participation is linked to steady-state behavior. It indicates that attention should be focused on how much the VSC can increase the voltage stability margin of the LCC in a steady state. The following sections lead to a clear understanding.

The highly transitory nature of CF phenomena may be quite complicated for analytical treatment because of system non-linearities. Added to the need for an exhaustive electromagnetic simulation to at least obtain statistics about the susceptibility of the CF, the search for a method that overcomes the difficulties listed so far and provides more reliable information is justified. From the next section on, this article presents a development that assumes that there are values for the ESCR for each system configuration such that a maximum γ excursion ($\Delta\gamma$) exists following an AC fault that will not cause a CF. If the γ drop at the inverter is greater than $\Delta\gamma$, the CF is presumed to occur. Figure 4 illustrates extinction angle behavior for two situations of Figure 1b and can help with understanding. Such boundary value for ESCR is influenced by control system gains, type of fault and harmonics, etc. The detailed mathematical analysis focuses on determining the maximum ESCR that could be reached in the LCC-HVDC busbar to which the inverter would be CF-protected for a given level of short circuit in MVA.

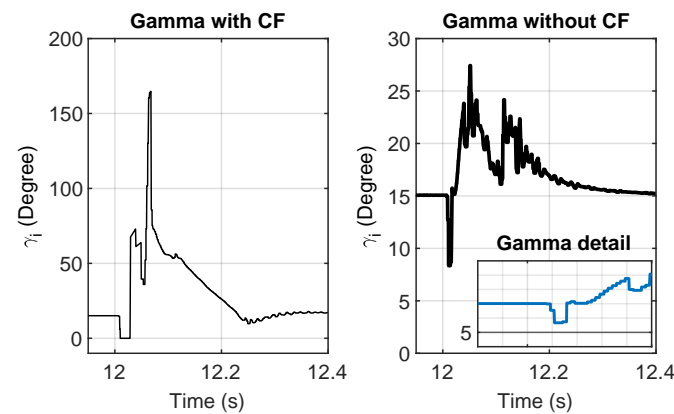


Figure 4. Graphic representation γ_i dynamics following AC fault.

3. Theoretical Analysis

3.1. VSC-HVDC Power/Voltage Relationships and LCC-HVDC Performance

The dependence of VSC-HVDC Power Common Coupling (PCC) voltage (V_k) on the dispatched powers is established to illustrate the influence of the VSC-HVDC in the *h*MIF system. The objective is to write V_k as a function of power dispatches on the VSC-HVDC terminals. The current I_k measured at the PCC can be written as (7), where E_k is the bridge-arm converter controllable voltage.

$$I_k = \frac{E_k - V_k}{Z_k} \quad (7)$$

So that the result can be applied in AC symmetrical and balanced systems with constant frequency and transient situations, the development is performed with all three-phase quantities written as two-component vectors (*dq*-frame). Therefore, all impedance will become static complex numbers with reactance as an imaginary component. The grid current is then,

$$I_{kd} + jI_{kq} = \frac{E_{kd} + jE_{kq} - V_{kd} - jV_{kq}}{R_k + jX_k} \quad (8)$$

The inductive reactance of the filtering and the transformer leakage reactance can be represented collectively by the interfacing reactor X_k . The AC bus voltage V_k is assumed with zero phase angle, aligned with *d*-axis. In this way, $V_{kq} = 0 \Rightarrow \vec{V}_{kdq} = V_{kd} = V_k$. Thus, after proper algebraic manipulations, the VSC complex power can be written as ((9)).

$$\vec{S}_k = 3V_k I_k^* = 3V_k \left(\frac{(E_{kd} - V_k)R_k + E_{kq}X_k}{R_k^2 + X_k^2} \right) + 3V_k \left(\frac{(E_{kd} - V_k)X_k - E_{kq}R_k}{R_k^2 + X_k^2} \right) \quad (9)$$

If the resistance is small enough that it can be neglected, V_k (assuming a converter-level firing system based on a simple sinusoidal pulse width modulation, the controllable converter voltage is $E_k = \sqrt{E_{kd}^2 + E_{kq}^2}$ on which components in the phasor domain are $E_{kd} = M_d \frac{V_{DC}}{2\sqrt{2}}$ and $E_{kq} = M_q \frac{V_{DC}}{2\sqrt{2}}$) is

$$V_k = \sqrt{\frac{E_k^2}{2} - Q_k X_k \pm \sqrt{\frac{E_k^4}{4} - X_k^2 P_k^2 - X_k E_k^2 Q_k}} \quad (10)$$

Equation (10) describes the correlation between V_k and VSC powers, which is graphically illustrated by the power-voltage curve. Explicitly dealing with a VSC, as V_k is controlled at 1 pu, the effect of the “nose” curve will be reflected in the other passive buses in the electrical vicinity of the bus k . This effect will be examined in detail in the following sections.

Figure 5 shows a system representation for studying the power exchange between VSC-HVDC and n LCC-HVDC subsystems. The premise that the power transmission system is predominantly inductive is adopted, that is, $\frac{X}{R} \gg 1$.

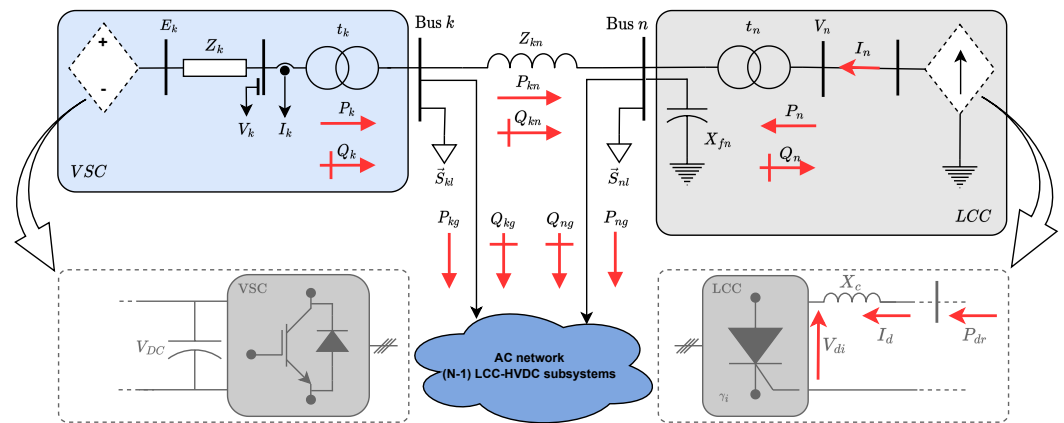


Figure 5. Representation of a three-bus hybrid multi-infeed system.

In this paper, the Hybrid Power Voltage Interaction Factor is defined. The $hPVIF_{nk}$ is a new parameter for estimating the degree of voltage interaction between a VSC-HVDC and the LCC-HVDC in an AC network and is defined as a function of the VSC-HVDC location and operating set point. Its value may be conveniently designed to protect the LCC-HVDC n for a given short circuit level.

3.2. Voltage Source Converters Operation and Control Modes

To proceed with the mathematical model, discussing the possible modes of operation of the VSC topology converters adopted in HVDC applications is convenient since the Jacobian elements depend on the VSC-HVDC inverter control mode. Regarding the active power control mode on both converters, the inverter station is designed to provide the active power demanded from the loads, intended to match the power dispatch order provided by the system operators. The rectifier station will be controlled to regulate the DC link voltage in preset reference, calculated according to the DC link storage energy.

Regarding the reactive power component, the AC bus voltage sending end is regulated by adjusting the field current of synchronous generators on that side so that the reactive order to the rectifier station is only set to zero. In the inverter station, the following control settings can be implemented.

- The inverter is designed to inject constant P into or keep constant Q in the AC network. This strategy is known as P -mode and Q -mode controls, respectively. It is not a recommended mode to operate in a weak grid because Q_k results from a composition of several effects, such as the tie line reactance, load conditions, and control set point, which affects the capability to regulate the AC voltage magnitude at a fixed value.
- By adjusting the output complex power, AC bus voltage magnitude is kept in a range of predetermined values, which is not acceptable to be less than 1 pu, nor should it exceed ten percent of the AC rating voltage. It is named PQ -control mode, on which Q reacts to P variations for the inverter AC bus terminal voltage to act as a PV bus. It is the control mode applied in this work.
- The inverter assumes a combined strategy of both controls as described in the previous items. However, an additional control loop to supplement the constant central reactive power control by inserting a voltage regulation control signal proportional to the RMS AC PCC voltage error is called the QV -droop control method.

3.3. Contribution Analysis of VSC in hMIF System

As noted in Section 2.5, the VSC's contribution to the CFII at the remote LCC depends on the ESCR in its AC converter bus, which is directly influenced by the VSC dispatch and tie line length. In other words, to extract benefits from the VSC-HVDC located in the EPS vicinity, it is more appropriate to analyze its contribution to steady-state voltage stability rather than the dynamics performance of the control during the fast transients.

As the behavior of interest is only the performance improvement of the LCC inverter side, the equations that describe the operation of the rectifier will not be depicted. The quasi-steady-state DC mathematical model of the inverter [56,57] is represented by the set of equations in Equation (11).

$$\begin{aligned}
 P_{di} &= V_{di} I_d \\
 V_{di} &= \frac{3\sqrt{2}}{\pi} n V_n \cos \gamma_i - \frac{3}{\pi} X_c I_d \\
 \cos \phi_i &= \frac{\cos \gamma_i - \cos(\gamma_i + \mu)}{2} \\
 Q_{di} &= P_{di} \operatorname{tg} \phi_i
 \end{aligned}
 \tag{11}$$

where P_{di} is the real power injection, V_{di} and I_d are direct voltage and current, respectively, n_t is the converter transformer tap ratio, γ_i , μ and are, respectively, the extinction and overlap angles, $\cos \phi_i$ is converter power factor, and Q_{di} is the reactive power consumption in converter and transformer. The system power flow equations for the system model are summarized as follows.

$$\begin{aligned}
 \Delta P_n &= P_{ng} + P_{nl} \pm P_{nk} - P_n \\
 \Delta Q_n &= Q_{ng} + Q_{nl} \pm Q_{nk} - Q_n + Q_{fn}
 \end{aligned}
 \tag{12}$$

In (12), ΔP_n and ΔQ_n are the vectors of AC active and reactive power incremental change, respectively, calculated on the AC bus of each inverter station. All quantities are given in pu and depicted in Figure 5. Subscript n and k refer to the LCC and VSC converters AC terminals, respectively, and subscript i refers to the LCC inverter station.

The LCC control mode adopted is the base case, which in the well-known current margin control corresponds to the rectifier controlling the voltage and the inverter terminal, the current, or equivalently the power, known as constant extinction angle (CEA). The fixed variables on the inverter are in the vector $[\alpha_r \gamma_i V_{di} I_d]$. Neglecting switching converter losses, $P_n = P_{di}$ is a function of AC and DC state variables. As the only behavior of interest is the V_n rise on the inverter, all P_{di} changes will be concurrently compensated by P_{dr} due to direct voltage V_{dr} in the rectifier side. In other words, the rectifier control will decrease α_r to increase V_{dr} and thus keep I_d constant. Figure 6 illustrates P_k from 0.05 to 0.75 pu and the V_n characteristic, while Figure 7 shows the corresponding DC variables.

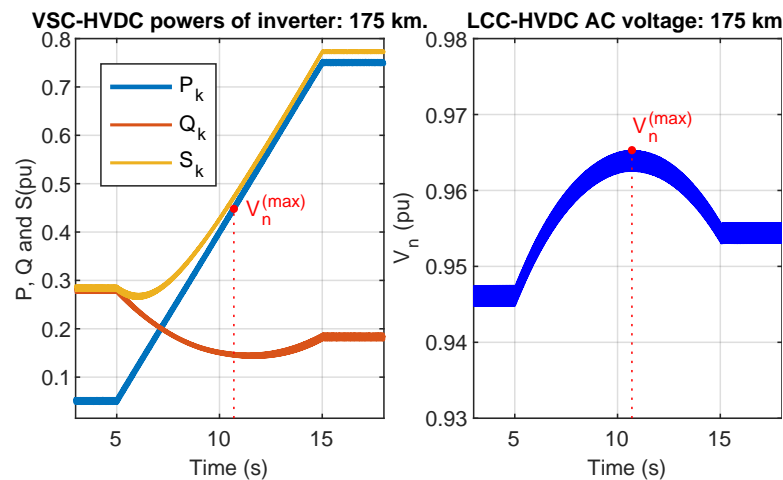


Figure 6. VSC power variations and LCC inverter AC bus voltage.

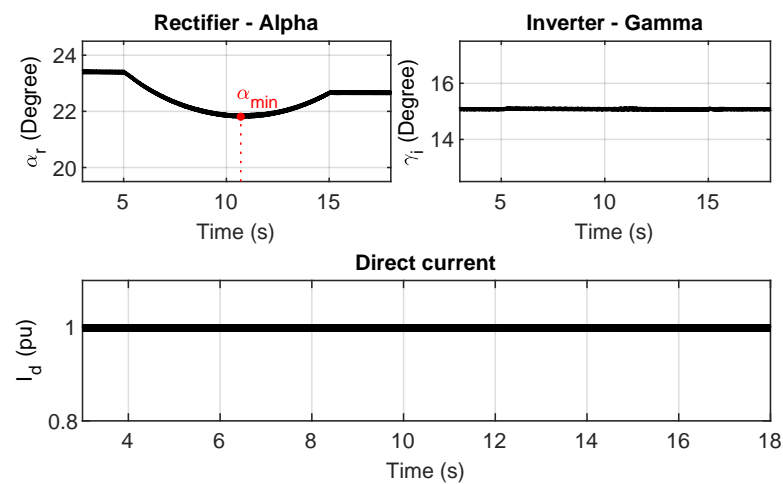


Figure 7. LCC-HVDC DC variables under VSC powers variations.

Such a result is denoted by the derivative of P_{di} concerning the V_n , as in (14). In addition, the participation of the state variables on the AC side is appropriately represented in the extended form of the Jacobian matrix of the linearized system power flow equations.

$$\frac{\partial P_{di}}{\partial V_n} = \frac{\partial}{\partial V_n} \left[\frac{3\sqrt{2}}{\pi} n_t V_n \cos \gamma_i I_d - \frac{3}{\pi} X_{cn} I_d^2 \right] \tag{13}$$

As for the increase in V_{di} , the value γ_i is constrained in $\gamma_{min} = 15^\circ$, and I_d is fixed in 1 pu—only those variations in the function of AC voltage are relevant. Then, the partial derivative in (14) can be calculated.

$$\begin{aligned} \frac{\partial P_{di}}{\partial V_n} &= \frac{3\sqrt{2}}{\pi} n_t \cos \gamma_i I_d \\ \frac{\partial Q_{di}}{\partial V_n} &= \frac{3\sqrt{2}}{\pi} n_t \cos \gamma_i I_d \operatorname{tg} \phi_i \\ \frac{\partial P_{di}}{\partial \gamma_i} &= \frac{\partial Q_{di}}{\partial \gamma_i} = 0 \\ \frac{\partial P_{di}}{\partial I_d} &= \frac{\partial Q_{di}}{\partial I_d} = 0 \end{aligned} \tag{14}$$

Equation (14) denotes that, strictly in this study, the AC power incremental changes ΔP_n and ΔQ_n in (12) are only sensitive to incremental changes in the AC state variables.

The canonical linear form $\mathbf{Ax}=\mathbf{b}$ of steady-state power–voltage relationships for the hybrid multi-infeed HVDC system is derived by the power flow equations stated in the AC/DC converter station [58]. In this way, the complete system already incorporating the DC elements is shown in (15), where \mathbf{A} is a real-valued matrix, and \underline{x} and \underline{b} are, respectively, the incremental changes in state variables and converter power vectors.

The matrix J is divided into N sub-matrices with self-explanatory notation and whose elements are the first partial derivatives of the power flow equations with respect to the state variables. The vector $\underline{Y}_d = [\gamma_i \ V_{di} \ I_d]$ with the DC variables is incorporated into the vector \underline{x} .

Thus, Equation (15) depicts the extended form, which can be generalized for all submatrices.

$$\begin{bmatrix} \Delta P_{(1)} \\ \vdots \\ \Delta P_{(N-1)} \\ \Delta P_{(N)} \\ \Delta P_{(k)} \\ \hline \Delta Q_{(1)} \\ \vdots \\ \Delta Q_{(N-1)} \\ \Delta Q_{(N)} \\ \Delta Q_{(k)} \end{bmatrix} = \begin{bmatrix} J_{P\delta} & & & & & & J_{PY_d} \\ \hline & J_{QV_{(1)}} & \cdots & J_{QV_{(N-1)}} & J_{QV_{(N)}} & J_{QV_{(k)}} & \\ \hline J_{Q\delta} & \vdots & \ddots & \vdots & \vdots & \vdots & J_{QY_d} \\ & J_{QV_{(N-1)}} & \cdots & J_{QV_{(N-1)}} & J_{QV_{(N)}} & J_{QV_{(k)}} & \\ & J_{QV_{(N)}} & \cdots & J_{QV_{(N-1)}} & J_{QV_{(N)}} & J_{QV_{(k)}} & \\ & J_{QV_{(k)}} & \cdots & J_{QV_{(N-1)}} & J_{QV_{(N)}} & J_{QV_{(k)}} & \end{bmatrix} \begin{bmatrix} \Delta\delta_{(1)} \\ \vdots \\ \Delta\delta_{(N-1)} \\ \Delta\delta_{(N)} \\ \Delta\delta_{(k)} \\ \hline \frac{\Delta V_{(1)}}{V_0} \\ \vdots \\ \Delta|V_{(N-1)}| \\ \Delta|V_{(N)}| \\ \Delta|V_{(k)}| \\ \hline \Delta Y_d \end{bmatrix} \tag{15}$$

The Jacobian submatrices $J_{P\delta}$, J_{PV} , $J_{Q\delta}$ and J_{QV} , where N and k are the total of LCC and VSC links nodes, respectively, are partial derivatives of the nonlinear algebraic functions

$$P_k = V_k \sum_{m \in k} V_m (G_{km} \cos \theta_{km} + B_{km} \sin \theta_{km}), \quad Q_k = V_k \sum_{m \in k} V_m (G_{km} \sin \theta_{km} - B_{km} \cos \theta_{km}) \tag{16}$$

$P_k = f_p(V, \theta)$ and $Q_k = f_q(V, \theta)$, in terms of the independent state variables AC voltage magnitude and phase angle in the form evaluated at the AC bus given by the active and reactive power flow [59,60]. Thus, the k th line is associated with the VSC-HVDC converter, and sub-index m denotes the AC LCC converter nodes and $m \in 1, 2, \dots, N$.

3.4. Enhancement of ESCR by VSC-HVDC

By incorporating modifications in the Jacobian to accommodate the VSC-HVDC and adjusting elements according to its respective control mode, this article addresses an extension of the [30,61]. Furthermore, as it also includes the effect of line length, this paper extends the previous work by considering a VSC included, particularly [62,63], in which the analysis of the degree of interaction is based on a dual infeed system only with LCC-HVDC. Based on a parametric study, the latter quantifies the direct gain in ESCR viewed from the LCC-HVDC AC busbar, yet it is only based on electromagnetic simulations and does so without presenting a mathematical formulation that can be generalized for any case.

The PQ mode control will be adopted as it is the only one with practical application for a realistic scenario when bus k is treated as a PV bus. The function V_n has been then described as a two-variable function on VSC powers. If there are partial derivatives, the concept of gradient vector will be applied and then is denoted by $\vec{\nabla} V_n(p_k, q_k)$ in (17).

$$\vec{\nabla} V_n = \begin{pmatrix} \frac{\partial V_n}{\partial P_k} & \frac{\partial V_n}{\partial Q_k} \end{pmatrix} \tag{17}$$

The powers P_k and Q_k are simultaneously controlled so that V_k is allowed to assume values within a well-defined band of acceptable node voltage magnitudes established by the power system operator. In this way, the following relationships in (18) are valid.

$$\frac{\partial V_k}{\partial P_k} = 0, \quad \frac{\partial V_k}{\partial Q_k} = 0 \tag{18}$$

In the next section, the $\vec{\nabla} V_n$ will be better explored and the $hPVIF$ is presented.

3.5. Approach: The Hybrid Power Voltage Interaction Factor (hPVIF)

This section explores the concept of the Hybrid Power Voltage Interaction Factor ($hPVIF$) for the dual $hMIF$ case. By employing the eigenvalue decomposition technique,

when the k th VSC-HVDC inverter station is operating in PQ -mode control, the corresponding $hPVIF_{nk}^{(p)}$ and $hPVIF_{nk}^{(q)}$ are defined from (19).

$$\begin{bmatrix} \Delta Q^{(1)} \\ \Delta Q^{(2)} \\ \Delta Q^{(3)} \\ \Delta P^{(1)} \\ \Delta P^{(2)} \\ \Delta P^{(3)} \end{bmatrix} = \begin{bmatrix} J_{QV_{11}} & J_{QV_{12}} & J_{QV_{13}} & J_{Q\delta_{11}} & J_{Q\delta_{12}} & J_{Q\delta_{13}} \\ J_{QV_{21}} & J_{QV_{22}} & J_{QV_{23}} & J_{Q\delta_{21}} & J_{Q\delta_{22}} & J_{Q\delta_{23}} \\ J_{QV_{31}} & J_{QV_{32}} & J_{QV_{33}} & J_{Q\delta_{31}} & J_{Q\delta_{32}} & J_{Q\delta_{33}} \\ J_{PV_{11}} & J_{PV_{12}} & J_{PV_{13}} & J_{P\delta_{11}} & J_{P\delta_{12}} & J_{P\delta_{13}} \\ J_{PV_{21}} & J_{PV_{22}} & J_{PV_{23}} & J_{P\delta_{21}} & J_{P\delta_{22}} & J_{P\delta_{23}} \\ J_{PV_{31}} & J_{PV_{32}} & J_{PV_{33}} & J_{P\delta_{31}} & J_{P\delta_{32}} & J_{P\delta_{33}} \end{bmatrix} \begin{bmatrix} \frac{\Delta|V_{(1)}|}{V_0} \\ \frac{\Delta|V_{(2)}|}{V_0} \\ 0 \\ \frac{\Delta\delta^{(1)}}{\Delta\delta^{(2)}} \\ 0 \end{bmatrix} \quad (19)$$

A sequence of algebraic operations in (19) allows the AC Reduced-Jacobian matrix J_R to turn into (20). The complete transformation is presented in Appendix A

$$hPVIF_{p_{nk}} = \frac{1}{J_{R_{kn}}^{(p)}}, \quad hPVIF_{q_{nk}} = \frac{1}{J_{R_{kn}}^{(q)}} \quad (20)$$

Figure 8 shows the composite surface, which is twisted-saddle shaped and will be of great importance in understanding the physical meaning of the $hPVIF_{nk}$. For every VSC set point, the V_n is determined in such a way that $\vec{\nabla}V_n(hPVIF_p, hPVIF_q)$ is valid at any point on the surface, as well as all of its mathematical properties. Two of the most important provide the direction of the greatest increase in V_n , which is perpendicular to the tangent line of the level curve, both in point $V_n(P_{k0}, Q_{k0})$. It is easily seen that the $hPVIF_{nk}$ provides a comprehensive mathematical interpretation for a cross-voltage sensitivity factor. In a simplified way, there is only an incremental change in \vec{S}_k , and then $hPVIF_{nk}$ establishes a direct relationship to a voltage change in the n th converter AC busbar. In this context, $hPVIF_{nk}$ will serve as a valuable primary metric for the subsequent voltage stability study of hybrid multi-infeed HVDC systems. It is not only the quantity $hPVIF_{nk}$ that is of importance, but it also carries information about how a power variation in one k busbar and its geographic location influences the voltage in another n busbar in the electrical vicinity of the system.

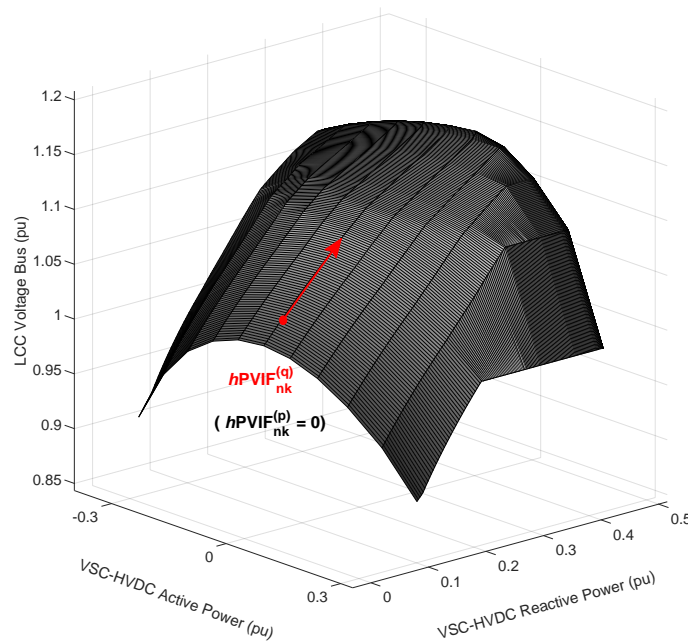


Figure 8. Three-dimensional view of the relation between \vec{S}_k and V_n .

3.6. The hPVIF Calculation

The strong relationship between V_n and the VSC set point and location has already been discussed, which leads to the hPVIF and iCFII indices being closely related.

Mathematically, $hPVIF_{nk}^{(p)}$ is the n th mode eigenvalue of the Jacobian matrix and is equivalent to the cross derivative that establishes a direct relationship between V_n to the electric distance between the buses n and k . For any VSC operating point, \vec{S}_k provides an expressive approximation of the critical point $V_{2_{max}}$ in time.

The V_n characteristic shows that its maximum occurs at $\partial V_n = 0$ for both $hPVIF_{nk}^{(p)}$, or in other words, only the numerator of $hPVIF_{nk}^{(p)}$ (denoted by $\mathcal{N}(hPVIF_{nk}^{(p)})$) is enough to study the interesting phenomena. Expanding the numerator results in a polynomial function in the form of (21), on which a is the set of constructive parameters of the AC grid, while independent variable x represents the operation points, and both will be used as input to the model.

$$\mathcal{N}(hPVIF_{nk}^{(p)})(a, x) = a_n \cdot x^n + a_{n-1} \cdot x^{n-1} + \dots + a_2 \cdot x^2 + a_1 \cdot x^1 + a_0 \quad (21)$$

Solving $\mathcal{N}(hPVIF_{nk}^{(p)})(a, x) = 0$ for the dependent variable V_n as a function of the independent variables P_k and Q_k results in second-order polynomials functions (22).

$$V_n^{(p)}(a, x) = \left(\sum_{i=n}^{n_4} a_i P_k^2 + \sum_{i=n_3}^{n_2} a_i P_k + \sum_{i=n_1}^{n_0} a_i \right)^{1/n} \quad (22)$$

where $n = n_1 + n_2 + n_3 + n_4$ is half the highest power of V_n , the vector of coefficients is $\underline{a} = [G_{km} \ B_{km} \ Y_{sh} \ \theta_{km} \ P_{2,3} \ Q_{2,3}]$ and $\underline{x} = [P_k \ Q_k]$. Bus 3 is the infinite bus, then, $V_3 = 1$ pu and $\theta_3 = 0$ rad, and all the other node voltage and phase-shifting angles are referenced to this one.

The scope of this work is restricted to the power system operating at a voltage regular operating point, according to the set of IEEE definitions regarding voltage stability [64]. In other words, an injection of reactive power $\Delta Q_k > 0$ at the VSC-HVDC AC bus leads to an increase (or at least not a decrease) in the voltage magnitude at all other system nodes, except the VSC AC bus itself due to the adopted control mode ($\Delta V_n \geq 0, n \neq k$ and $\Delta V_k = 0$). Therefore, the index $hPVIF_{nk}^{(q)}$ does not apply to the analysis on which V_n is calculating through $hPVIF_{nk}^{(q)} = 0$ since the power system will operate away from the point of voltage collapse (Figure 8).

Since the $hPVIF_{nk}$ equations describe a physical system, the following considerations are stated:

- By definition, the $hPVIF_{nk}$ corresponds to a critical point. Since V_n goes from increasing to decreasing at a time instant in which $\Delta V_n = 0$, this is a local maximum.
- Physical constraints force the independent variable $P_k \in \mathbb{R}_+^*$.
- The quantities P_3 and Q_3 are determined by the system operator, being fixed inputs for $V_n(a, x)$ for any line lengths.

In summary, the section shows that it is possible to calculate the real and imaginary powers coordinates in the VSC to achieve the maximum ESCR in the LCC link, which means the upper limit of the voltage stability margin. The threshold V_n that provides the maximum possible ESCR (maximum $\Delta\gamma$) for each specified tie line length. In other words, the eigenvalue $\lambda = hPVIF_{nk}$ contains valuable information not only on the maximum ESCR that can be reached for each line length but also delimits the region of instability, calculating the point from which P_k values cause a reduction in SCR.

4. Technical Data of the hMIF System Topology

To carry out the simulations to validate the proposed hPVIF and its derived contributions, a typical scheme of a hybrid dual-infeed HVDC system is established in a

PSCAD/EMTDC electromagnetic transients (EMT) program. Its configurations and control structure employed in each HVDC subsystem are discussed as follows.

4.1. LCC-HVDC

Accurate EMTP models of the LCC and VSC converters are addressed in this section.

The LCC-HVDC and VSC-HVDC units' ratings are summarized in Table 1. The LCC-HVDC link adopts the first CIGRÉ HVDC benchmark standard testing system [65,66], widely applied over the decades as a standard reference and effective tool for HVDC system studies [67,68].

Table 1. HVDC constructive and operating parameters.

Parameter	VSC-HVDC	LCC-HVDC
System rating (MVA)	1000	1000
Converter AC bus rated voltage (kV)	230	230
DC rated voltage (kV)	630	500
DC side	-	R = 5 Ω
	C = 0.25 mF	L = 1.2 H C = 26 μF
Rectifier station		
Switching frequency (Hz)	-	50
Capacitor banks and shunt filter Capacity	-	11th order: 252 Mvar 13th order: 252 Mvar Capacitors: 125 Mvar
Converter transformer leakage reactance (pu)	0.19	0.18
Transformer turns ratio	62.5/13.8 kV	345/213.5 kV
AC system	345 kV, 50 Hz	
SCR	-	2.5 at 84°
Inverter station		
Switching frequency (Hz)	-	50
Capacitor banks and shunt filter Capacity	-	11th order: 252 Mvar 13th order: 252 Mvar Capacitors: 125 Mvar
Converter transformer leakage reactance (pu)	0.19	0.18
Transformer turns ratio	62.5/230 kV	230/209.23 kV
AC system	215.05 kV, 50 Hz	
SCR	-	1.75 at 75°

4.2. VSC-HVDC

In this VSC-HVDC point-to-point model, the real power dispatch and the AC voltage regulation are achieved using the pq theory [69], described in (23). The Instantaneous Power Theory—or $p-q$ Theory—is defined by applying the Clarke Transformation in AC voltages and currents in the time domain. The terms p^* and q^* are the power components in the $\alpha\beta$ stationary reference frame.

The powers p and q are real and imaginary, respectively. Both are defined by average and oscillating components $p = \bar{p} + \tilde{p}$ and $q = \bar{q} + \tilde{q}$, and the instantaneous complex power results from $\vec{s} = p + jq$. Since distortions and imbalances in voltages and currents are out of scope, the oscillating components \tilde{p} and \tilde{q} will be null, and only the fundamental frequency is considered.

Figure 9 illustrates the block diagram of the two-layer dq control scheme. The outer power control loop is noticed by $g_d(s)$ and $g_q(s)$ regulators and receives real power (or a DC voltage) and AC voltage references, according to the selector switch. The output current i_d^* is generated and denotes the average real power (\bar{p}) that should be provided to (inverter) or absorbed from (rectifier) the AC network to ensure the DC link voltage regulation, while i_q^* is associated with necessary reactive power (\bar{q}) required to control PCC voltage. The output voltage components of the inner vector current loop $h_d(s)$ and $h_q(s)$ pass through a dq -to- abc -frame transformation block to generate the reference (v_{abc})

to be synthesized at the AC converter side. Both layers are composed of conventional proportional integral controllers.

The DC cable represents an overhead line, whose length is fixed at 1000 km, and the AC line connecting buses k and n , whose length can be varied as desired. All these quantities will be evident in Figure 9. Harmonics and switching problems are out of the scope of this work; thus, the VSC is modeled as a three-phase voltage source in this work, i.e., IGBT devices are not used [70].

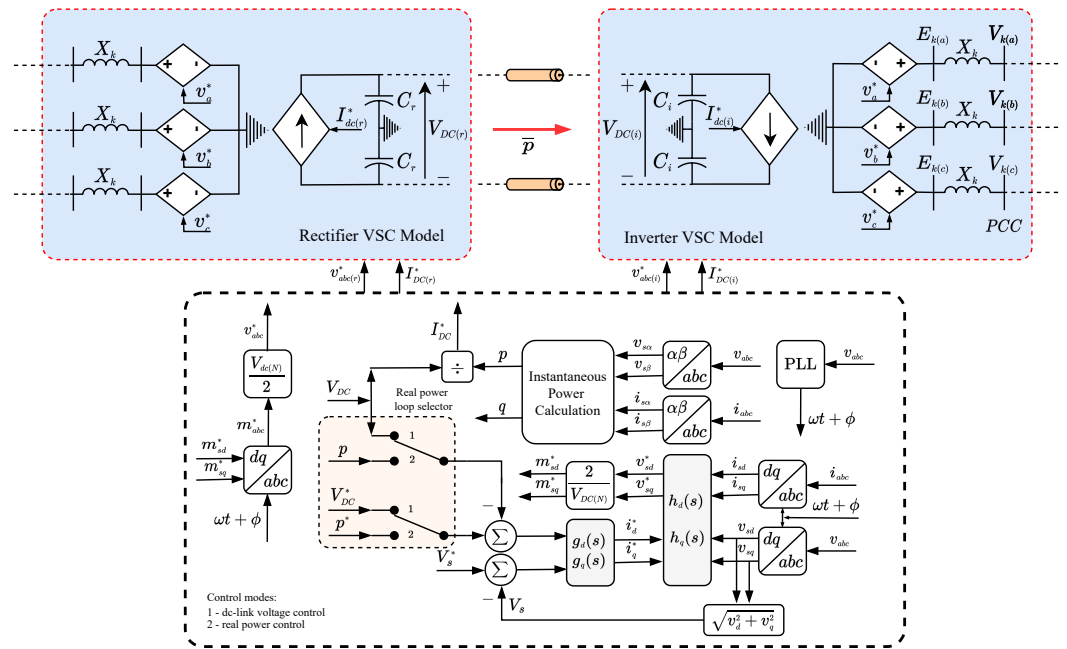


Figure 9. Grid interface of the VSC model and its vector control scheme.

The related parameters of the control system are given in Table 2.

Table 2. Control circuit parameters.

Parameter	Gain	Time Constant
$h_d(s)$	2	617 μ s
$h_q(s)$	0.1	4 ms
$g_d(s)$	5	7.5 ms
$g_q(s)$	10	7.5 ms

$$\begin{bmatrix} i_\alpha^* \\ i_\beta^* \end{bmatrix} = \frac{1}{v_\alpha^2 + v_\beta^2} \begin{bmatrix} v_\alpha & v_\beta \\ v_\beta & -v_\alpha \end{bmatrix} \cdot \begin{bmatrix} p^* \\ q^* \end{bmatrix} \quad (23)$$

4.3. AC Grid Topology

The AC voltage source is modeled as a Thévenin equivalent. The LCC link scaled version has source impedance parameters adjusted to achieve the appropriated ESCR. Table 3 lists AC network parameters such as the voltage and frequency ratings and power capacities.

Table 3. AC grid parameters.

Parameter	Value
Rated power (MVA)	1000
Rated voltage (kV)	230
Rated frequency (Hz)	50
Transmission line	Frequency-Dependent (Phase) Model

5. Simulations Results

Among those transient aspects strongly influenced by the ESCR in LCC systems, the commutation failure susceptibility is considered for the validity verification of the calculation method of the *h*PVIF.

5.1. Improved Immunity to Commutation Failure

The central idea is to study the impacts on the CFII caused by the presence of a VSC-HVDC and its direct contribution to the ESCR through a steady-state aspect. By proposing the auxiliary index *i*CFII, the influence of the VSC-HVDC will be studied according to a steady-state aspect, through the measuring of the static voltage stability margin, which is its operating point, analyzed from the instantaneous complex power vector in the plane.

The fault level can be per-unitized by dividing it by the rated DC power of LCC-HVDC. In this work, CFII is per-unitizing the CF fault level and is described in (24).

$$CFII = \frac{\text{Worst critical fault (MVA)}}{P_{dn}} \times 100 = \frac{V_n^2}{\omega \cdot L_{min} \cdot P_{dc}} \times 100 \quad (24)$$

The inductance L_{min} (H) is the smallest fault inductance that never results in a CF, regardless of fault type [45], and ω the angular frequency in rad/s for 50 Hz.

5.1.1. Evaluation Method of *i*CFII

In [71], it is demonstrated that CF is influenced not only by the fault level but also by the point on the commutation voltage wave at which the short circuit is applied. Furthermore, it is shown that the higher susceptibility to CF occurs under an inductive three-phase fault than other fault types or impedance.

Starting from a small value, the fault inductance is increased in increments of 0.5 mH until it reaches a value where no CF is induced for a period of 20 ms. A set of twelve faults is uniformly distributed in time for each inductance, applying every 1.666 ms for such an inductance value.

$$360/12 = 30^\circ \implies \frac{30^\circ \times f}{360^\circ} = 1.6667 \text{ ms}$$

To demonstrate the sensitivity of *i*CFII to the length of the transmission line segment, Table 4 shows the profile of CFII considering the variation only in the line length and keeping the active power dispatch fixed at 0.7 pu. Although the CFII is in percentage values, the authors chose to show *i*CFII in MVA.

Table 4. Local CFII values in the *h*MIF system—line length.

Length (km)	V_n (pu)	CFII (%)	P_k (pu)	Q_k (pu)	<i>i</i> CFII (MVA)
same bus	0.9949	24.159	0.7	0.3261	36.862
25	0.9798	23.666	0.7	0.2685	31.939
50	0.9704	23.258	0.7	0.2283	27.853
75	0.9648	23.162	0.7	0.2045	26.893
100	0.9607	22.436	0.7	0.1910	19.640
125	0.9579	22.557	0.7	0.1850	20.843
150	0.9554	22.318	0.7	0.1808	18.451
175	0.9534	22.054	0.7	0.1771	15.820
200	0.9516	21.968	0.7	0.1761	14.957
225	0.9501	21.925	0.7	0.1791	14.528
250	0.9489	21.883	0.7	0.1746	14.101
275	0.9477	21.897	0.7	0.1664	14.243
300	0.9464	21.826	0.7	0.1683	13.533
325	0.9451	21.505	0.7	0.1725	10.328
350	0.9439	21.355	0.7	0.1768	8.828

In order to verify the VSC performance, Table 5 shows the behavior of the *i*CFII by incorporating the VSC power dispatch to each of the tie line lengths. In this way, the effect of the real power dispatch will be superimposed on every line length, which P_k will be the

one related to the point of $hPVIF_{nk}^{(p)} = 0$. It is also included a column of the $hPVIF_{nk}^{(q)}$, in which will be a helpful index for the concept introduced in the next section.

Table 5. Local CFII values in the *h*MIF system—VSC complex power.

Length (km)	$hPVIF_{nk}^{(p)}$	$hPVIF_{nk}^{(q)}$	$V_n^{(c)}$ (pu)	V_n (pu) ¹	ϵ (%) ²	P_k (pu)	Q_k (pu)	CFII (%)	<i>i</i> CFII (MVA)
same bus	0.003	0.396	0.9969	0.9955	0.148	0.3354	0.3546	24.368	38.960
25	0.009	0.198	0.9806	0.9821	0.152	0.3406	0.2797	23.716	32.439
50	0.012	0.396	0.9769	0.9745	0.766	0.3334	0.2357	23.306	28.336
75	0.012	0.593	0.9656	0.9706	0.506	0.3379	0.2095	23.082	26.099
100	0.012	0.790	0.9673	0.9683	0.098	0.3462	0.1914	22.739	22.670
125	0.011	0.986	0.9659	0.9669	0.105	0.3423	0.1787	22.602	21.297
150	0.011	1.182	0.9641	0.9669	0.287	0.3394	0.1706	22.422	19.491
175	0.006	1.374	0.9706	0.9653	0.547	0.3712	0.1549	22.332	18.599
200	0.004	1.567	0.9650	0.9649	0.003	0.3694	0.1487	22.185	17.128
225	0.002	1.758	0.9698	0.9647	0.528	0.3340	0.1516	22.332	18.599
250	0.001	1.948	0.9653	0.9646	0.075	0.3686	0.1380	22.112	16.399
275	−0.001	2.136	0.9609	0.9645	0.372	0.3337	0.1411	21.982	15.100
300	−0.003	2.323	0.9601	0.9646	0.469	0.3350	0.1360	21.997	15.244
325	−0.005	2.508	0.9593	0.9648	0.569	0.3355	0.1320	21.911	14.385
350	−0.006	2.691	0.9667	0.9650	0.179	0.3379	0.1267	21.812	13.392

^c Calculated V_n from (22). ¹ Simulated values of V_n . ² Relative error of $V_n^{(c)}$.

Figure 10 illustrates the V_n dependence on the tie line length and VSC power dispatch. The impact on CFII in *h*MIF systems is graphically represented by the hatched area. For every length, the vertical distance between the red dotted line and solid line denotes the real gain of CFII, or *i*CFII, by just connecting the VSC at operating point $P_k = 0.7$ pu (scenario under consideration in Table 4). The vertical distance between the solid line and the line with point markers is the *i*CFII considering those P_k related to $hPVIF_{nk}^{(p)} = 0$ (scenario under consideration in Table 5). The superscripts with a single and double asterisk mean VSC connected with fixed and variant \tilde{S}_k , respectively.

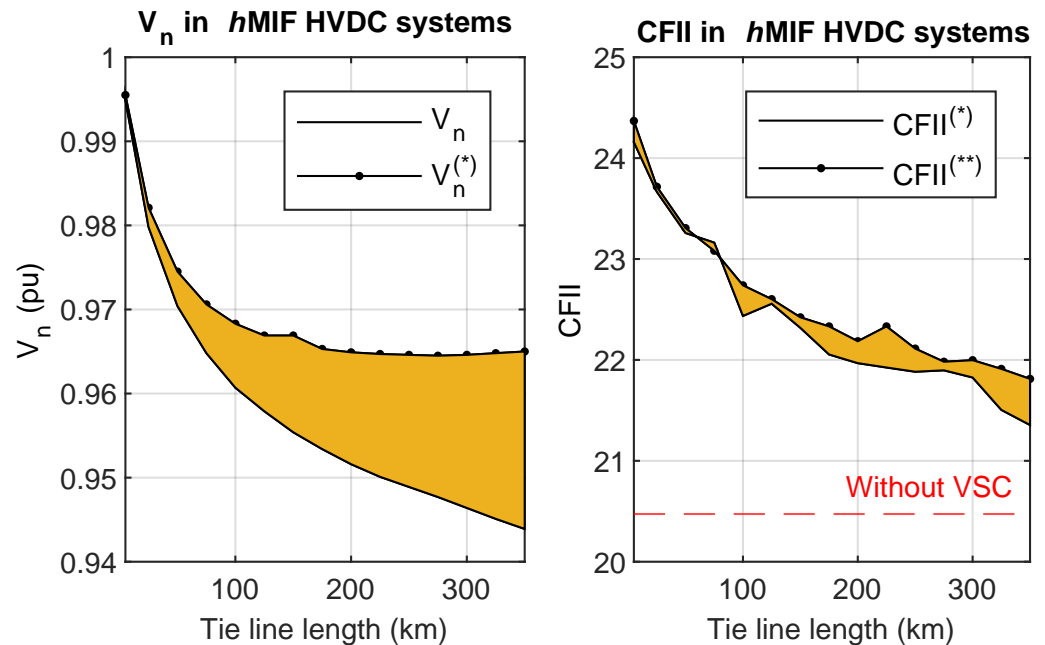
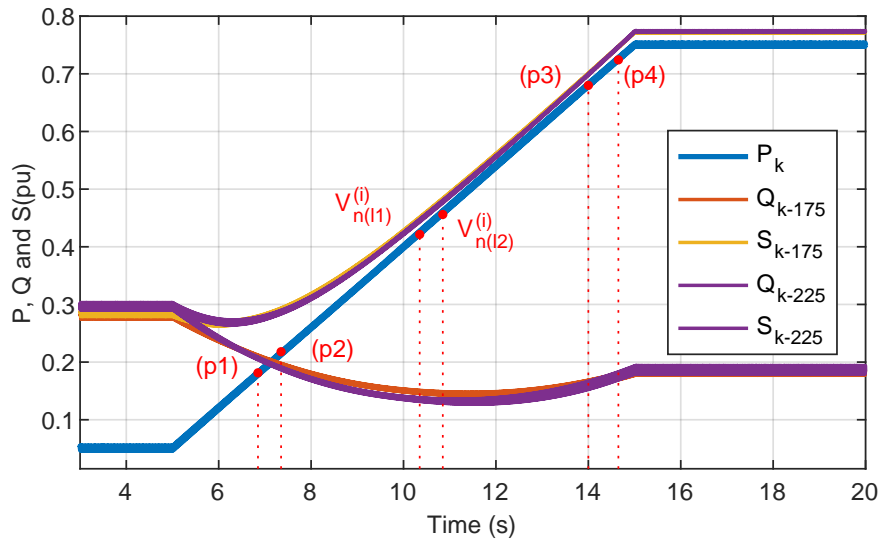


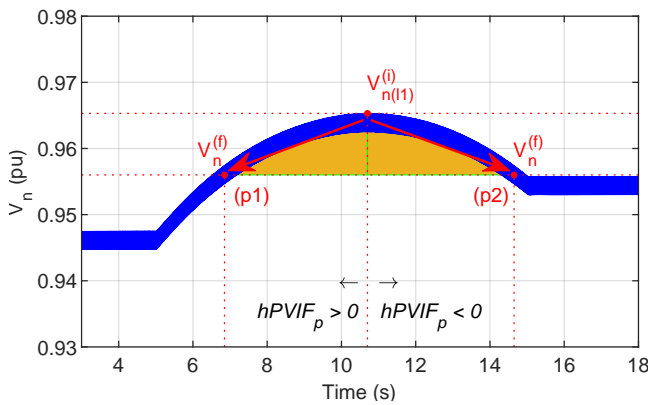
Figure 10. Impact of VSC on V_n and CFII in *h*MIF systems.

In addition to the definition of Section 5.1.1, the CF immunity quantified by the CFII is not absolute but relative to a given short-circuit level. If for a given AC bus voltage the LCC-HVDC system is immune to such short-circuit level in MVA, it is also immune to all voltages above this first voltage. Figure 11b,c brings a further graphical representation of

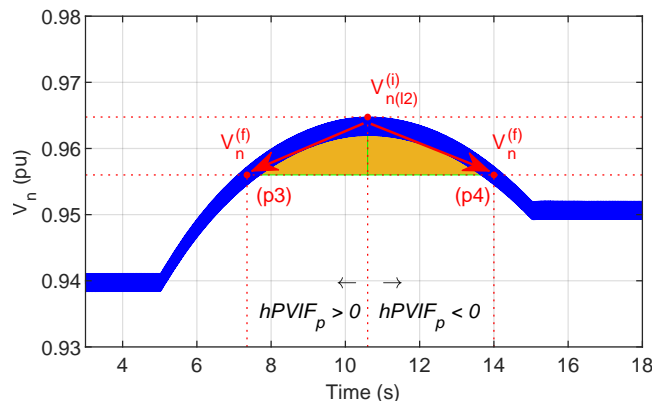
the *i*CFII phenomenon. All voltage values in the range between $V_n^{(f)}$ (hatched area) will return CFII equal to and greater than the maximum value itself ($V_n^{(i)}$).



(a)



(b)



(c)

Figure 11. LCC-HVDC inverter station AC bus voltage as function of \vec{S}_k : (a) VSC-HVDC powers of inverter station. (b) LCC-HVDC AC voltage for 175 km. (c) AC LCC Voltage for 225 km.

Figure 11 complements the understanding of what has been presented so far, in addition to supporting the discussion of the next section.

5.1.2. Apparent Line Length through *h*PVIF

Equation (22) can not be used to calculate V_n at any time since the referred equations derive from the boundary condition $\partial V_n = 0$. Then it is valid only at the maximum V_n . The use of the eigenvalues $hPVIF_{nk}^{(p)}$ and $hPVIF_{nk}^{(q)}$ as complementary indexes is explored in this section.

This section introduces the concept of the apparent line length of the transmission line seen from the AC side of the LCC-HVDC inverter. By choosing the proper Q_k (and thus P_k), it is possible to simulate a shorter line length than the actual length, resulting in a higher value of *i*CFII. This is proved as follows.

Considering a given Q_k for two line lengths l_1 and l_2 , with $l_1 < l_2$, then $V_{n(l_1)} > V_{n(l_2)}$, as shown in Figure 11. Therefore, to match the effect of varying power dispatch on different line lengths, the two final voltages of interest must be equal, as in Equation (25).

$$V_{n(l_2)}^{(f)} = V_{n(l_1)}^{(f)} \implies \Delta V_{n(l_2)} = V_{n(l_1)}^{(i)} - V_{n(l_2)}^{(i)} + \Delta V_{n(l_1)} \quad (25)$$

Equation (A4) results in the following:

$$Q_{k(l_2)}^{(f)} = \left[V_{n(l_1)}^{(i)} - V_{n(l_2)}^{(i)} + \Delta V_{n(l_1)} \right] hPVIF_{nk}^{(q)} \Big|_{l_2}^{(-1)} + Q_{k(l_2)}^{(i)} \quad (26)$$

Or,

$$Q_{k(l_2)}^{(f)} = \left[V_{n(l_1)}^{(i)} - V_{n(l_2)}^{(i)} + \Delta Q_{k(l_1)} hPVIF_{nk}^{(q)} \Big|_{l_1} \right] hPVIF_{nk}^{(q)} \Big|_{l_2}^{(-1)} + Q_{k(l_2)}^{(i)} \quad (27)$$

In (27), the superscript (i) indicates quantities associated with the maximum point, and the subscript (f) is related to that point on which the quantity of interest is desired. The value $\Delta Q_{k(l_2)}$ establishes the necessary reactive power on bus k for l_2 that would result in the same $iCFII$ for l_1 when $Q_{k(l_1)}$ is delivered.

Since $hPVIF_{nk}^{(p)}$ is null at the maximum point, it could not be directly used in apparent line length. However, it is helpful for $hPVIF_{nk}^{(q)}$ calculation since the latter is nonzero at that point. The practical result of the first term of the equation is to emulate, in a simplified way, a shorter line length by adjusting Q_k power dispatch.

Because of the large number of tie line length combinations, the concept of apparent line length will be demonstrated for only two lengths: 175 and 225 km, being therefore extensible to all pairs of line lengths. Figure 11b,c show the tie line equivalence for the lengths chosen when P_k is adjusted from 0.05 to 0.75 pu and Q_k values necessary for equivalence is presented in Table 6.

Table 6. Apparent line length equivalence between 175 and 225 km.

Region	V_n (pu) ¹	Q_k (pu) ¹	$Q_k^{(c)}$ (pu)	e (%) ²
$hPVIF_{nk}^{(p)} > 0$	0.9560	0.1901	0.1880	1.126
$hPVIF_{nk}^{(p)} < 0$	0.9560	0.1616	0.1615	0.0368

¹ Simulated values of Q_k . ^c Calculated Q_k from (27). ² Relative error of $Q_k^{(c)}$.

5.2. Discussion and Partial Conclusions

Intended for the assessment of voltage static stability in hybrid multi-infeed HVDC systems, this study is vital to the power system and power electronics fields combined since it addresses a valuable open topic related to the LCC-HVDC connection into the grid with low short circuit capacity.

The results presented corroborate the mathematical statements and physical conclusions exposed through Sections 3 and 5. The CF is an adverse condition associated with a weak system, and the AC voltage deterioration is quite sensitive to tie line length and VSC power dispatch. These results attest to the effectiveness of the index $hPVIF_{nk}^{(p)}$ as a predictor of the maximum ESCR that could be provided for a given line length and operating point. It is also observed that LCC-HVDC is more susceptible to propagating CF when LCC and VSC inverters operate at long electrical distances from each other.

As a form of validation, Tables 4 and 5 show an additional column with the error obtained for the voltage value at the maximum point from e (%) = $(|V_n - V_n^{(c)}|) / V_n \times 100$, where the superscript c refers to the value calculated through (22). Such errors can be attributed to (1) numerical approximations, mainly rounding errors, since the representation of values relative to state variables was limited to four decimal places, (2) approximations inherent to the bus admittance matrix, and (3) due to model assumptions such as when

separately assuming $\Delta Q = 0$ and $\Delta P = 0$ for $hPVIF_{nk}$ calculations. This is valid for applying the gradient concept, but it is not a very accurate assumption for a physical system since to keep $V_k = 1$, $\Delta Q = 0$ and $\Delta P = 0$ cannot be decoupled.

6. Conclusions

This paper introduced a new metric to evaluate the degree of influence of the VSC-HVDC on inhibiting commutation failures in LCC-HVDC systems arising from AC faults from the increase in the ESCR. A detailed theoretical analysis is developed considering VSC-HVDC participation factors $hPVIF_{nk}^{(p)}$ and $hPVIF(q)_{nk}$ and its associated contributions intended for the assessment of voltage static stability in hybrid multi-infeed HVDC systems. It is possible to obtain satisfactory results with the proposed method as a function of VSC-HVDC operation set point and line length separation. Commutation failures and most of their adverse consequences could be avoided when the LCC-HVDC operates at the calculated maximum short circuit capacity.

Oriented computer simulations performed in PSCAD/EMTDC denote the validity of the proposed method. Results indicate close correspondence between the simulation-based results and the predicted results from the analytical expressions. The parametric analysis provided in Section 5 was carried out using ranges of tie line length and VSC-HVDC power dispatch. To support the findings, Tables 4 and 5 show that values of $iCFII$ corresponding to $hPVIF_{nk}^{(p)} = 0$ reflect the ability of the VSC-HVDC to improve AC voltage regulation, enhance the overall system strength and make the LCC-HVDC less susceptible to commutation failure.

The presented technique proved efficient at increasing system performance and has become technically convenient as a voltage static stability evaluation tool. In this context, based on daily, weekly, or longer time horizon orders, the system operator can predict the impact on the dynamic behavior of the ESCR when there are changes in the network and when EPS assumes different modes of operation to meet consumer demands.

Through proper choice of VSC-HVDC set points, the outcomes of this work show that the apparent line length formulation also reveals considerable accuracy in emulating more advantageous line lengths from an ESCR improvement point of view. It is a valuable concept not only for supporting the new transmission line projects and expansion at the planning stage but also as an enhanced tool for operation engineers dealing with short and long-term decisions, providing elements for the precise application of preventive measures that contribute to the safe integration of LCC-HVDC and VSC-HVDC to very weak AC grids.

Author Contributions: Conceptualization, D.O.; methodology, D.O.; validation, D.O. and G.C.B.L.; writing—original draft preparation, D.O., G.C.B.L. and D.H.; writing—review and editing, D.O., G.C.B.L., D.H., M.A., E.G.-D. and J.M.C.; project administration, M.A.; funding acquisition, M.A. All authors have read and agreed to the published version of the manuscript.

Funding: This research was funded by the CAPES (Higher Education Personnel Improvement Coordination—Brazil)—Finance Code 001, the CNPQ (National Council for Scientific and Technological Development—Brazil) and by the European Union—NextGenerationEU—University of Seville, grant number MSALAS-2022-19823.

Data Availability Statement: Not Applicable.

Acknowledgments: Thanks to the Universidad de Sevilla for the contributions and for providing support from professors and students and to the Federal University of Rio de Janeiro for providing equipment and physical structure. The researchers express gratitude to the national and international authorities for funding the project and the LEMT group from the University of Rio de Janeiro.

Conflicts of Interest: The authors declare no conflict of interest.

Appendix A. Equations for hPVIF Calculation

The hPVIF_{nk}^(p) and hPVIF_{nk}^(q) Calculation

In V -control mode, V_k is maintained constant for any changes in P_k , V_n is nonzero, and Q_k will be automatically adjusted to changes in P_k not only to meet the operator's dispatch but also to meet the stated target of $\Delta V_k = 0$.

Complete Jacobian matrix considering slack bus (bus 3) in power flow formulation ($\Delta V_{(3)}$ and $\Delta\delta_{(3)}$).

$$\begin{bmatrix} \Delta Q_{(1)} \\ \Delta Q_{(2)} \\ \Delta Q_{(3)} \\ \Delta P_{(1)} \\ \Delta P_{(2)} \\ \Delta P_{(3)} \end{bmatrix} = \begin{bmatrix} \mathbf{L} = J_{QV} & \mathbf{M} = J_{Q\delta} \\ \mathbf{N} = J_{PV} & \mathbf{H} = J_{P\delta} \end{bmatrix} \begin{bmatrix} \frac{\Delta|V_{(1)}|}{V_0} \\ \frac{\Delta|V_{(2)}|}{V_0} \\ \frac{\Delta|V_{(3)}|}{V_0} \\ \Delta\delta_{(1)} \\ \Delta\delta_{(2)} \\ \Delta\delta_{(3)} \end{bmatrix} \quad (\text{A1})$$

1—Elimination of bus 3: First Kron reduction

In this step, the non-interest AC buses, such as the Thevenin equivalent source buses, have already been eliminated. As $\Delta V_{(3)}$ and $\Delta\delta_{(3)}$ are null, the equation above becomes.

$$\begin{bmatrix} \Delta Q_{(1)} \\ \Delta Q_{(2)} \\ \Delta Q_{(3)} \\ \Delta P_{(1)} \\ \Delta P_{(2)} \\ \Delta P_{(3)} \end{bmatrix} = \begin{bmatrix} J_{QV_{11}} & J_{QV_{12}} & J_{QV_{13}} & J_{Q\delta_{11}} & J_{Q\delta_{12}} & J_{Q\delta_{13}} \\ J_{QV_{21}} & J_{QV_{22}} & J_{QV_{23}} & J_{Q\delta_{21}} & J_{Q\delta_{22}} & J_{Q\delta_{23}} \\ J_{QV_{31}} & J_{QV_{32}} & J_{QV_{33}} & J_{Q\delta_{31}} & J_{Q\delta_{32}} & J_{Q\delta_{33}} \\ J_{PV_{11}} & J_{PV_{12}} & J_{PV_{13}} & J_{P\delta_{11}} & J_{P\delta_{12}} & J_{P\delta_{13}} \\ J_{PV_{21}} & J_{PV_{22}} & J_{PV_{23}} & J_{P\delta_{21}} & J_{P\delta_{22}} & J_{P\delta_{23}} \\ J_{PV_{31}} & J_{PV_{32}} & J_{PV_{33}} & J_{P\delta_{31}} & J_{P\delta_{32}} & J_{P\delta_{33}} \end{bmatrix} \begin{bmatrix} \frac{\Delta|V_{(1)}|}{V_0} \\ \frac{\Delta|V_{(2)}|}{V_0} \\ 0 \\ \Delta\delta_{(1)} \\ \Delta\delta_{(2)} \\ 0 \end{bmatrix} \quad (\text{A2})$$

In preparation for the elimination of bus 3 (slack bus), the following sequence of operations will be performed for a first Kron reduction: (1) Permutation of the 3rd and 5th rows to place $\Delta Q_{(3)}$ and $\Delta P_{(3)}$ in the fifth and sixth lines of vector \underline{b} , respectively. (2) Permutation of the 3rd and 5th columns to place $\Delta V_{(3)}$ and $\Delta\delta_{(3)}$ in the last two lines of vector \underline{x} , and (3) permutation of the 1st and 2nd columns to place $\Delta V_{(2)}$ in the first row of vector \underline{x} .

$$\begin{bmatrix} \Delta Q_{(1)} \\ \Delta Q_{(2)} \\ \Delta P_{(2)} \\ -\Delta P_{(1)} \\ -\Delta Q_{(3)} \\ \Delta P_{(3)} \end{bmatrix} = \begin{bmatrix} J_{QV_{12}} & J_{QV_{11}} & J_{QV_{13}} & J_{Q\delta_{13}} & J_{Q\delta_{12}} & J_{Q\delta_{11}} \\ J_{PV_{32}} & J_{PV_{31}} & J_{PV_{33}} & J_{P\delta_{33}} & J_{P\delta_{32}} & J_{P\delta_{31}} \\ J_{QV_{32}} & J_{QV_{31}} & J_{QV_{33}} & J_{Q\delta_{33}} & J_{Q\delta_{32}} & J_{Q\delta_{31}} \\ J_{PV_{12}} & J_{QV_{21}} & J_{PV_{13}} & J_{P\delta_{13}} & J_{P\delta_{12}} & J_{P\delta_{11}} \\ J_{PV_{22}} & J_{PV_{21}} & J_{PV_{23}} & J_{P\delta_{23}} & J_{P\delta_{22}} & J_{P\delta_{21}} \\ J_{QV_{22}} & J_{PV_{11}} & J_{QV_{23}} & J_{Q\delta_{23}} & J_{Q\delta_{22}} & J_{Q\delta_{21}} \end{bmatrix} \begin{bmatrix} \frac{\Delta|V_{(2)}|}{V_0} \\ \frac{\Delta|V_{(1)}|}{V_0} \\ \Delta\delta_{(2)} \\ -\Delta\delta_{(1)} \\ 0 \\ 0 \end{bmatrix} \quad (\text{A3})$$

After the matrix inversion in (A3), followed by the first Kron reduction, a second matrix inversion is performed, resulting in (A4).

$$\begin{bmatrix} \Delta Q_{(1)} \\ \Delta Q_{(2)} \\ \Delta P_{(2)} \\ \Delta P_{(1)} \end{bmatrix} = \begin{bmatrix} J_{QV_{12}}^{(r1)} & J_{QV_{11}}^{(r1)} & J_{Q\delta_{12}}^{(r1)} & J_{Q\delta_{11}}^{(r1)} \\ J_{QV_{12}}^{(r1)} & J_{QV_{11}}^{(r1)} & J_{Q\delta_{12}}^{(r1)} & J_{Q\delta_{11}}^{(r1)} \\ J_{PV_{22}}^{(r1)} & J_{PV_{21}}^{(r1)} & J_{P\delta_{22}}^{(r1)} & J_{P\delta_{21}}^{(r1)} \\ J_{PV_{12}}^{(r1)} & J_{PV_{11}}^{(r1)} & J_{P\delta_{12}}^{(r1)} & J_{P\delta_{11}}^{(r1)} \end{bmatrix} \begin{bmatrix} \frac{\Delta|V_{(2)}|}{V_0} \\ \frac{\Delta|V_{(1)}|}{V_0} \\ \Delta\delta_{(2)} \\ \Delta\delta_{(1)} \end{bmatrix} \quad (\text{A4})$$

To formalize the mathematical basis of this article and to make it possible to obtain hPVIF_p and hPVIF_q directly from (A5), the coordinate Q will be constrained as a constant

parameter so that the directional derivative on the P axis is calculated. Physically, to decouple the effects of the active power variations from those caused by reactive power incremental changes, it is firstly suggested in [26] to assume $\Delta Q = 0$ and $\Delta P = 0$ separately. With no reactive power injections, the last Kron reduction can be applied.

$$\begin{bmatrix} \Delta Q_{(1)} \\ \Delta Q_{(2)} \end{bmatrix} = \begin{bmatrix} J_{QV_{12}}^{(r2)} & J_{QV_{11}}^{(r2)} \\ J_{QV_{22}}^{(r2)} & J_{QV_{21}}^{(r2)} \end{bmatrix} \begin{bmatrix} \frac{\Delta|V_{(2)}|}{V_0} \\ \frac{\Delta|V_{(1)}|}{V_0} \end{bmatrix} \quad (\text{A5})$$

As this article deals with a dual h MIF system, from now on, the sub-indices n for LCC and k for VSC ($k = 1$ and $n = 2$) will be adopted. As $\Delta|V_{(10)}| = 0$, considering Equation (A6) and using J_R generic terms, the system is rewritten as:

$$\begin{bmatrix} \Delta Q_{(k)} \\ \Delta Q_{(n)} \end{bmatrix} = \begin{bmatrix} J_{R_{kn}}^{(q)} & J_{R_{kk}}^{(q)} \\ J_{R_{nn}}^{(q)} & J_{R_{nk}}^{(q)} \end{bmatrix} \begin{bmatrix} \Delta|V_{(n)}| \\ 0 \end{bmatrix} \quad (\text{A6})$$

$$\Delta Q_{(k)} = J_{R_{kn}}^{(q)} \Delta V_{(n)} + 0 \Rightarrow \frac{\Delta V_{(n)}}{\Delta Q_{(k)}} = \frac{1}{J_{R_{kn}}^{(q)}} \quad (\text{A7})$$

$$hPVIF_{q_{nk}} = \frac{1}{J_{R_{kn}}^{(q)}} \quad (\text{A8})$$

Similar methodology is applied in (A4) with proper permutations to calculate $hPVIF_p$.

$$\begin{bmatrix} \Delta P_{(k)} \\ \Delta P_{(n)} \end{bmatrix} = \begin{bmatrix} J_{R_{kn}}^{(p)} & J_{R_{kk}}^{(p)} \\ J_{R_{nn}}^{(p)} & J_{R_{nk}}^{(p)} \end{bmatrix} \begin{bmatrix} \Delta|V_{(n)}| \\ 0 \end{bmatrix} \quad (\text{A9})$$

$$\Delta P_{(k)} = J_{R_{kn}}^{(p)} \Delta V_{(n)} + 0 \Rightarrow \frac{\Delta V_{(n)}}{\Delta P_{(k)}} = \frac{1}{J_{R_{kn}}^{(p)}} \quad (\text{A10})$$

$$hPVF_{p_{nk}} = \frac{1}{J_{R_{kn}}^{(p)}} \quad (\text{A11})$$

References

1. EMPRESA, D.P.E. Plano Decenal de Expansão de Energia 2031. Ministério de Minas e Energia–Secretaria de Planejamento e Desenvolvimento Energético. Brasília–DF–Brasil. 2022. Available online: <https://www.epe.gov.br/pt/publicacoes-dados-abertos/publicacoes/plano-decenal-de-expansao-de-energia-2031> (accessed on 11 November 2022).
2. Shu, T.; Lin, X.; Peng, S.; Du, X.; Chen, H.; Li, F.; Tang, J.; Li, W. Probabilistic power flow analysis for hybrid HVAC and LCC-VSC HVDC system. *IEEE Access* **2019**, *7*, 142038–142052. [CrossRef]
3. Ainsworth, J.; Gavrilovic, A.; Thanawala, H. Static and synchronous compensators for HVDC transmission convertors connected to weak AC systems. In Proceedings of the 28th Session CIGRE, Paris, France, 27 August–4 September 1980; p. 31-01.
4. Nayak, O.B.; Gole, A.; Chapman, D.; Davies, J. Dynamic performance of static and synchronous compensators at an HVDC inverter bus in a very weak AC system. *IEEE Trans. Power Syst.* **1994**, *9*, 1350–1358. [CrossRef]
5. Zhang, F.; Xin, H.; Wu, D.; Wang, Z.; Gan, D. Assessing strength of multi-infeed LCC-HVDC systems using generalized short-circuit ratio. *IEEE Trans. Power Syst.* **2018**, *34*, 467–480. [CrossRef]
6. Khazaei, J.; Idowu, P.; Asrari, A.; Shafaye, A.; Piyasinghe, L. Review of HVDC control in weak AC grids. *Electr. Power Syst. Res.* **2018**, *162*, 194–206. [CrossRef]
7. Xue, Y.; Zhang, X.P.; Yang, C. Elimination of commutation failures of LCC HVDC system with controllable capacitors. *IEEE Trans. Power Syst.* **2015**, *31*, 3289–3299. [CrossRef]
8. Xue, Y.; Zhang, X.P. Reactive power and AC voltage control of LCC HVDC system with controllable capacitors. *IEEE Trans. Power Syst.* **2016**, *32*, 753–764. [CrossRef]
9. Xue, Y.; Zhang, X.P.; Yang, C. Commutation failure elimination of LCC HVDC systems using thyristor-based controllable capacitors. *IEEE Trans. Power Deliv.* **2017**, *33*, 1448–1458. [CrossRef]
10. Wei, Z.; Yuan, Y.; Lei, X.; Wang, H.; Sun, G.; Sun, Y. Direct-current predictive control strategy for inhibiting commutation failure in HVDC converter. *IEEE Trans. Power Syst.* **2014**, *29*, 2409–2417. [CrossRef]

11. Liu, L.; Lin, S.; Sun, P.; Liao, K.; Li, X.; Deng, Y.; He, Z. A calculation method of pseudo extinction angle for commutation failure mitigation in HVDC. *IEEE Trans. Power Deliv.* **2019**, *34*, 777–779. [[CrossRef](#)]
12. Wang, Q.; Zhang, C.; Wu, X.; Tang, Y. Commutation failure prediction method considering commutation voltage distortion and DC current variation. *IEEE Access* **2019**, *7*, 96531–96539. [[CrossRef](#)]
13. Mirsaeidi, S.; Dong, X. An enhanced strategy to inhibit commutation failure in line-commutated converters. *IEEE Trans. Ind. Electron.* **2019**, *67*, 340–349. [[CrossRef](#)]
14. Wei, Z.; Fang, W.; Liu, J. Variable extinction angle control strategy based on virtual resistance to mitigate commutation failures in HVDC system. *IEEE Access* **2020**, *8*, 93692–93704. [[CrossRef](#)]
15. Liu, Y.; Chen, Z. A flexible power control method of VSC-HVDC link for the enhancement of effective short-circuit ratio in a hybrid multi-infeed HVDC system. *IEEE Trans. Power Syst.* **2013**, *28*, 1568–1581. [[CrossRef](#)]
16. Qahraman, B. Series/Parallel Hybrid VSC-LCC for HVdc Transmission Systems. Ph.D. Thesis, Electrical and Computer Engineering, University of Manitoba, Winnipeg, MB, Canada, 2010.
17. Portugal, P.M.M. Transmissão em Corrente Contínua com Tecnologia Híbrida Multiterminal de Conversores Fonte de Tensão e Corrente. Ph.D. Thesis, Tese de Doutorado, Universidade Federal do Rio de Janeiro (UFRJ)/COPPE, Rio de Janeiro, Brazil, 2015.
18. Xue, Y. Modelling and Control of Hybrid LCC HVDC System. Ph.D. Thesis, University of Birmingham, Birmingham, UK, 2016.
19. Fischer de Toledo, P. Modelling and Control of a Line-commutated HVDC Transmission System Interacting with a VSC STATCOM. Ph.D. Thesis, KTH Royal Institute of Technology, Stockholm, Sweden, 2007.
20. Flourentzou, N.; Agelidis, V.G.; Demetriades, G.D. VSC-based HVDC power transmission systems: An overview. *IEEE Trans. Power Electron.* **2009**, *24*, 592–602. [[CrossRef](#)]
21. Bucher, M.K.; Wiget, R.; Andersson, G.; Franck, C.M. Multiterminal HVDC networks—What is the preferred topology? *IEEE Trans. Power Deliv.* **2013**, *29*, 406–413. [[CrossRef](#)]
22. Renedo, J.; Garcia-Cerrada, A.; Rouco, L. Reactive-power coordination in VSC-HVDC multi-terminal systems for transient stability improvement. *IEEE Trans. Power Syst.* **2016**, *32*, 3758–3767. [[CrossRef](#)]
23. Gui, Y.; Wang, X.; Blaabjerg, F.; Pan, D. Control of grid-connected voltage-source converters: The relationship between direct-power control and vector-current control. *IEEE Ind. Electron. Mag.* **2019**, *13*, 31–40. [[CrossRef](#)]
24. Irnawan, R.; da Silva, F.F.; Bak, C.L.; Lindefelt, A.M.; Alefragkis, A. A droop line tracking control for multi-terminal VSC-HVDC transmission system. *Electr. Power Syst. Res.* **2020**, *179*, 106055. [[CrossRef](#)]
25. de Oliveira, D.d.S.; de Souza, M.J.A.; Leal, G.C.B.; Alves, F.A.L.; Aredes, M. Probabilistic assessment of the vsc-hvdc contribution in voltage stability applied to a hybrid dc-multi-infeed scenario. In Proceedings of the IECON 2020 the 46th Annual Conference of the IEEE Industrial Electronics Society, Singapore, 18–21 October 2020; pp. 1684–1691.
26. Löf, P.A.; Hill, D.J.; Arnborg, S.; Andersson, G. On the analysis of long-term voltage stability. *Int. J. Electr. Power Energy Syst.* **1993**, *15*, 229–237. [[CrossRef](#)]
27. Morison, G.; Gao, B.; Kundur, P. Voltage stability analysis using static and dynamic approaches. *IEEE Trans. Power Syst.* **1993**, *8*, 1159–1171. [[CrossRef](#)]
28. Aik, D.L.H.; Andersson, G. Power stability analysis of multi-infeed HVDC systems. *IEEE Trans. Power Deliv.* **1998**, *13*, 923–931. [[CrossRef](#)]
29. Aik, D.H.; Andersson, G. Use of participation factors in modal voltage stability analysis of multi-infeed HVDC systems. *IEEE Trans. Power Deliv.* **1998**, *13*, 203–211. [[CrossRef](#)]
30. Aik, D.L.H.; Andersson, G. Analysis of voltage and power interactions in multi-infeed HVDC systems. *IEEE Trans. Power Deliv.* **2013**, *28*, 816–824. [[CrossRef](#)]
31. Xia, C.; Li, X.; Li, S.; Zhou, B. Definition and analysis of receiving system voltage support strength factor. *IEEE Access* **2019**, *7*, 134206–134214. [[CrossRef](#)]
32. Ni, X.; Gole, A.M.; Zhao, C.; Guo, C. An improved measure of AC system strength for performance analysis of multi-infeed HVdc systems including VSC and LCC converters. *IEEE Trans. Power Deliv.* **2017**, *33*, 169–178. [[CrossRef](#)]
33. Xiao, H.; Li, Y. Multi-Infeed voltage interaction factor: A unified measure of inter-inverter interactions in hybrid multi-infeed HVDC systems. *IEEE Trans. Power Deliv.* **2019**, *35*, 2040–2048. [[CrossRef](#)]
34. Liu, J.; Chen, Z.; Wang, X. Influence of coupling characteristics on commutation failure of new hybrid HVDC transmission system. *IOP Conf. Ser. Earth Environ. Sci.* **2021**, *647*, 012025. [[CrossRef](#)]
35. Wei, Z.; Liu, J.; Fang, W.; Hou, J.; Xiang, Z. Commutation failure analysis in single-and multi-infeed HVDC systems. In Proceedings of the 2016 IEEE PES Asia-Pacific Power and Energy Engineering Conference (APPEEC), Xi’an, China, 25–28 October 2016; pp. 2244–2249.
36. Xia, C.; Suo, M.; Liang, X. Analysis on commutation failure caused by AC faults in multi-infeed HVDC systems. In Proceedings of the 2012 Power Engineering and Automation Conference, Wuhan, China, 18–20 September 2012; pp. 1–4.
37. Chen, X.; Gole, A.M.; Guo, C. A fast calculation method for the local commutation failure immunity indices in single-and multi-infeed HVDC systems. In Proceedings of the 11th IET International Conference on AC and DC Power Transmission, Birmingham, UK, 10–12 February 2015; pp. 1–6.
38. Tang, M.; Ma, L.; Zhang, B.; Wu, C.; Wang, L.; Li, E.; Chu, X. Optimal placement of dynamic reactive power compensation devices for improving immunity to commutation failure in multi-infeed HVDC systems. In Proceedings of the 2017 4th International Conference on Systems and Informatics (ICSAI), Hangzhou, China, 11–13 November 2017; pp. 247–251.

39. Xiao, H.; Li, Y.; Duan, X. Efficient approach for commutation failure immunity level assessment in hybrid multi-infeed HVDC systems. *J. Eng.* **2017**, *2017*, 719–723. [[CrossRef](#)]
40. Shao, Y.; Zhou, Q.; Sun, Y.; Tang, Y. A Simplified Index of Fast Evaluation of Commutation Failure Risk in Multi-infeed HVDC Systems. In Proceedings of the 2018 International Conference on Power System Technology (POWERCON), Guangzhou, China, 6–8 November 2018; pp. 42–47.
41. Thio, C.; Szechtman, M.; Silva, R. Simulation tests On commutation failure theory in HVDC systems. In Proceedings of the International Colloquium on HVDC and FACTS (CIGRE SC14), Montreal, QC, Canada, 17–19 September 1995.
42. Thio, C.; Davies, J.; Kent, K. Commutation failures in HVDC transmission systems. *IEEE Trans. Power Deliv.* **1996**, *11*, 946–957. [[CrossRef](#)]
43. Rahimi, E.; Gole, A.; Davies, J.; Fernando, I.; Kent, K. Commutation failure and overvoltage phenomena in multi-infeed HVDC systems. In Proceedings of the Colloquium of Role of HVDC, FACTS and Emerging Technologies in Evolving Power Systems, Bangalore, India, 17–24 September 2005; pp. 54–73.
44. Rahimi, E.; Gole, A.; Davies, J.; Fernando, I.; Kent, K. Commutation failure in single-and multi-infeed HVDC systems. In Proceedings of the 8th IEE International Conference on AC and DC Power Transmission, London, UK, 28–31 March 2006; pp. 182–186.
45. Rahimi, E.; Gole, A.; Davies, J.; Fernando, I.T.; Kent, K. Commutation failure analysis in multi-infeed HVDC systems. *IEEE Trans. Power Deliv.* **2010**, *26*, 378–384. [[CrossRef](#)]
46. Xiao, H.; Li, Y.; Zhu, J.; Duan, X. Efficient approach to quantify commutation failure immunity levels in multi-infeed HVDC systems. *IET Gener. Transm. Distrib.* **2016**, *10*, 1032–1038. [[CrossRef](#)]
47. Zhu, Y.; Zhang, S.; Liu, D.; Zhu, L.; Zou, S.; Yu, S.; Sun, Y. Prevention and mitigation of high-voltage direct current commutation failures: A review and future directions. *IET Gener. Transm. Distrib.* **2019**, *13*, 5449–5456. [[CrossRef](#)]
48. Lips, H. Aspects of multiple infeed of HVDC inverter stations into a common AC system. *IEEE Trans. Power Appar. Syst.* **1973**, *PAS-92*, 775–779. [[CrossRef](#)]
49. Mohan, N. *Power Electronics: A First Course*; Wiley: Hoboken, NJ, USA, 2011.
50. Bui, L.; Sood, V.; Laurin, S. Dynamic interactions between HVDC systems connected to AC buses in close proximity. *IEEE Trans. Power Deliv.* **1991**, *6*, 223–230. [[CrossRef](#)]
51. Bayo-Salas, A.; Beerten, J.; Rimez, J.; Van Hertem, D. Analysis of control interactions in multi-infeed VSC HVDC connections. *IET Gener. Transm. Distrib.* **2016**, *10*, 1336–1344. [[CrossRef](#)]
52. CIGRE. *System with Multiple dc Infeed*; CIGRÉ WG B4-41 Guide; CIGRE: Paris, France, 2008.
53. Shao, Y.; Tang, Y. Fast evaluation of commutation failure risk in multi-infeed HVDC systems. *IEEE Trans. Power Syst.* **2018**, *33*, 646–653. [[CrossRef](#)]
54. Hwang, S.; Lee, J.; Jang, G. HVDC-system-interaction assessment through line-flow change-distribution factor and transient-stability analysis at planning stage. *Energies* **2016**, *9*, 1068. [[CrossRef](#)]
55. IEEE Working Group. *IEEE Guide for Planning DC Links Terminating at AC Locations Having Low Short-Circuit Capacities*; Institute of Electrical and Electronics Engineers, Inc.: New York, NY, USA, 1997.
56. Arrillaga, J.; Watson, N.R.; Liu, Y. *Flexible Power Transmission: The HVDC Options*; John Wiley & Sons: Hoboken, NJ, USA, 2007.
57. Jovcic, D. *High Voltage Direct Current Transmission: Converters, Systems and DC Grids*; John Wiley & Sons: Hoboken, NJ, USA, 2019.
58. Monticelli, A.J.; Garcia, A. *Introdução a Sistemas de Energia Elétrica*; Ed Unicamp: Campinas, SP, Brazil, 2003.
59. Saadat, H. *Power System Analysis*; WCB/McGraw-Hill: New York, NY, USA, 1999.
60. Monticelli, A.J. *Fluxo de Carga em redes de Energia Elétrica*; E. Blucher: Sudbury, ON, Canada, 1983.
61. Aik, D.L.H.; Andersson, G. Fundamental analysis of voltage and power stability of single-infeed voltage-source converter HVDC systems. *IEEE Trans. Power Deliv.* **2018**, *34*, 365–375. [[CrossRef](#)]
62. Guo, C.; Zhang, Y.; Gole, A.M.; Zhao, C. Analysis of dual-infeed HVDC with LCC–HVDC and VSC–HVDC. *IEEE Trans. Power Deliv.* **2012**, *27*, 1529–1537. [[CrossRef](#)]
63. Rehman, B.; Rehman, A.u.; Khan, W.A.; Sami, I.; Ro, J.S. Operation and Challenges of Multi-Infeed LCC–HVDC System: Commutation Failure, AC/DC Power Flow, and Voltage Stability. *Appl. Sci.* **2021**, *11*, 8637. [[CrossRef](#)]
64. Bose, A.; Concordia, C.; Dunlop, R.D.; Fouad, A.A.; Kundur, P.; Schulz, R.P. Proposed Terms and Definitions for Power System Stability. *IEEE Trans. Power App. Syst.* **1982**, *101*, 1894–1898.
65. Szechtman, M.; Wess, T.; Thio, C. A benchmark model for HVDC system studies. In Proceedings of the International Conference on AC and DC Power Transmission, London, UK, 17–20 September 1991; pp. 374–378.
66. Faruque, M.; Zhang, Y.; Dinavahi, V. Detailed modeling of CIGRE HVDC benchmark system using PSCAD/EMTDC and PSB/SIMULINK. *IEEE Trans. Power Deliv.* **2005**, *21*, 378–387. [[CrossRef](#)]
67. Mazouz, L.; Zidi, S.A.; Hafaiifa, A.; Hadjeri, S.; Khatir, M.; Brahimi, L. Effect of commutation failures in a CIGRE model for HVDC link connected to AC network. In Proceedings of the 2018 International Conference on Applied Smart Systems (ICASS), Medea, Algeria, 24–25 November 2018; pp. 1–6.
68. Liu, P.; Che, R.; Xu, Y.; Zhang, H. Detailed modeling and simulation of+ 500kV HVDC transmission system using PSCAD/EMTDC. In Proceedings of the 2015 IEEE PES Asia-Pacific Power and Energy Engineering Conference (APPEEC), Brisbane, Australia, 15–18 November 2015; pp. 1–3.

69. Akagi, H.; Watanabe, E.H.; Aredes, M. *Instantaneous Power Theory and Applications to Power Conditioning*; John Wiley & Sons: Hoboken, NJ, USA, 2017; Volume 62.
70. van der Meer, A.A.; Gibescu, M.; van der Meijden, M.A.; Kling, W.L.; Ferreira, J.A. Advanced hybrid transient stability and EMT simulation for VSC-HVDC systems. *IEEE Trans. Power Deliv.* **2014**, *30*, 1057–1066. [[CrossRef](#)]
71. Rahimi, E. *Voltage Interactions and Commutation Failure Phenomena in Multi-Infeed HVDC Systems*; University of Manitoba: Winnipeg, MB, Canada, 2011.

Disclaimer/Publisher's Note: The statements, opinions and data contained in all publications are solely those of the individual author(s) and contributor(s) and not of MDPI and/or the editor(s). MDPI and/or the editor(s) disclaim responsibility for any injury to people or property resulting from any ideas, methods, instructions or products referred to in the content.